MSDS SKY REFERENCE AND PREAMPLIFIER STUDY

Final Report

Exhibit C

by

L. Larsen, S. Stewart, and P. Lambeck
Infrared and Optics Division

ENVIRONMENTAL RESEARCH INSTITUTE OF MICHIGAN
FORMERLY WILLOW RUN LABORATORIES, THE UNIVERSITY OF MICHIGAN

March 1974

prepared for

NATIONAL AERONAUTICS AND SPACE ADMINISTRATION
Johnson Space Center, Houston, Texas 77058
Earth Observations Division
Contract NAS 9-9784 Exhibit C

NOTICES

Sponsorship. The work reported herein was conducted by the Environmental Research Institute of Michigan for the National Aeronautics and Space Administration, Johnson Space Center, Houston, Texas 77058, under Contract NAS 9-9784, Exhibit C. James Kessel (EB-8) is Project Manager. Contracts and grants to the Institute for the support of sponsored research are administered through the Office of Contracts Administration.

Disclaimers. This report was prepared as an account of Government-sponsored work. Neither the United States, nor the National Aeronautics and Space Administration (NASA), nor any person acting on behalf of NASA:

(A) Makes any warranty or representation, expressed or implied with respect to the accuracy, completeness, or usefulness of the information contained in this report, or that the use of any information, apparatus, method, or process disclosed in this report may not infringe privately owned rights; or

(B) Assumes any liabilities with respect to the use of, or for damages resulting from the use of any information, apparatus, method, or process disclosed in this report.

As used above, "person acting on behalf of NASA" includes any employee or contractor of NASA, or employee of such contractor, to the extent that such employee or contractor of NASA or employee of such contractor prepares, disseminates, or provides access to any information pursuant to his employment or contract with NASA, or his employment with such contractor.

Availability Notice. Requests for copies of this report should be referred to:

National Aeronautics and Space Administration
Scientific and Technical Information Facility
P. O. Box 33
College Park, Maryland 20740

Final Disposition. After this document has served its purpose, it may be destroyed. Please do not return it to the Environmental Research Institute of Michigan.

TECHNICAL REPORT STANDARD TITLE PAGE

1. Report No.	2. Government Accession No.	3. Recipient's Catalog No.
~~NASA CR-ERIM 190100-1-F~~		

4. Title and Subtitle	5. Report Date
MSDS SKY REFERENCE AND PREAMPLIFIER STUDY	March 1974
	6. Performing Organization Code

7. Author(s)	8. Performing Organization Report No.
L. Larsen, S. Stewart, and P. Lambeck	ERIM 190110-1-F

9. Performing Organization Name and Address	10. Work Unit No.
Environmental Research Institute of Michigan Infrared and Optics Division P. O. Box 618 Ann Arbor, Michigan 48107	Exhibit C
	11. Contract or Grant No. NAS 9-9784
	13. Type of Report and Period Covered Final Report 1 November 1972 - 1 September 1973

12. Sponsoring Agency Name and Address	14. Sponsoring Agency Code
National Aeronautics and Space Administration Johnson Space Center Earth Observations Division Houston, Texas 77058	

15. Supplementary Notes

James Kessel/EB-8 is Project Manager for NASA

16. Abstract

The multispectral scanner is beyond the initial stages of development but is not yet an operational tool. The "Multispectral Scanner and Data System (MSDS)" was fabricated for NASA to be used as a research tool in order to develop techniques for implementation on the operational model. In keeping with this philosophy, a theoretical and experimental study was undertaken to develop and evaluate an improved Sky Reference and preamplifier design. Based on this study, a new Sky Reference system and a new preamplifier concept are recommended for incorporation into the MSDS.

17. Key Words	18. Distribution Statement
Multispectral scanner Multispectral scanner and data system (MSDS) Sky reference and preamplifier Remote sensing Environment Automatic data processing Aircraft Satellite	Initial distribution is listed at the end of this document.

19. Security Classif. (of this report)	20. Security Classif. (of this page)	21. No. of Pages	22. Price
UNCLASSIFIED	UNCLASSIFIED	64	6.50

PREFACE

This report describes part of a comprehensive and continuing program of research concerned with advancing the state-of-the-art in remote sensing of the environment from aircraft and satellites. The research is being carried out for NASA's Lyndon B. Johnson Space Center, Houston, Texas, by the Environmental Research Institute of Michigan (ERIM), formerly the Willow Run Laboratories of The University of Michigan. The basic objective of this multidisciplinary program is to develop remote sensing as a practical tool to provide the planner and decision-maker with extensive information quickly and economically.

Timely information obtained by remote sensing can be important to such people as the farmer, the city planner, the conservationist, and others concerned with problems such as crop yield and disease, urban land studies and development, water pollution, and forest management. The scope of our program includes the following: (1) extending the understanding of basic processes; (2) discovering new applications, developing advanced remote-sensing systems, and improving automatic data processing to extract information in a useful form; and (3) assisting in data collection, processing, analysis, and ground-truth verification.

The research described herein was performed under Contract NAS 9-9784, Exhibit C, and covers the period from 1 November 1972 to 1 September 1973. James Kessel has been the Project Manager. The program was directed by R. R. Legault, Vice President of the Institute, and by L. M. Larsen, Principal Investigator and Head of ERIM's Electronic Development Section. The Institute's number for this report is 190110-1-F. The authors wish to acknowledge the experimental work conducted at ERIM by J. Wiseman and N. Griffin.

CONTENTS

FIGURES

TABLES

MSDS SKY REFERENCE AND PREAMPLIFIER STUDY

1
SUMMARY

As the use of remote sensing data has been refined, the need for the refinement of sensor calibration has increased. The major goals in re-designing the Multispectral Scanner and Data System (MSDS) sky reference are: (1) to remove the sun-elevation angle and aircraft-attitude angle dependence from the solar-sky illumination measurement, and (2) to obtain data on the optical state of the atmosphere. The present sky reference is dependent on solar elevation and provides essentially no information on important atmospheric parameters. We expect that a measurement of sky illumination without solar illumination will allow a prediction to be made of path radiance and transmission as a function of wavelength. New sky sensors have been conceived for the MSDS which meet these goals and which can be evaluated on both a theoretical and experimental basis. Our recommendations for the implementation of an improved sky reference sensor are based on these evaluations.

Basically, we have tested two designs. One system is built around a hyperbolic mirror and the reflection approach. The curvature of the mirror is used to compensate for the so-called "cosine effect" of the sun angle. A hole at the center of the mirror permits the scanner to look through the mirror at a small diffusing disk which collects the energy reflected off the mirror. Although it satisfies almost all the design goals and has the best signal-to-noise ratio, this design has the disadvantages of large size, poor durability, and inability to view the sun within a $\pm 10^{\circ}$ of zenith because of view hole and collecting-diffuser vignetting.

A second approach to a sky reference utilizes a fish-eye lens to obtain a 180° field of view. We tested both an integrating sphere and opal glass as a means of diffusing the energy collected by the lens. Though it is much smaller, is easier to fabricate, and has unobscured vision for 180°, the fish-eye lens has a slightly poorer flatness of response (versus scan angle) and signal-to-noise than that of the mirror. A detailed re-design by JSC of the present sky reference around the fish-eye approach, even with its limitations, is hereby recommended for the MSDS system.

A preamplifier study was undertaken to find ways of improving the noise-equivalent reflectance by reducing the noise level for silicon detector channels on the MSDS. We made a theoretical and experimental evaluation on the original circuit of the delivered preamplifiers and on the first stage of an improved hybrid preamplifier. A fivefold improvement with the hybrid has been measured with a detector operating at the full bandwidths required for the MSDS at maximum V/H = 0.18. A larger improvement is expected when operating at a reduced bandwidth with lower V/H.

We propose that the Array 1 circuitry of the MSDS be modified to include a hybrid stage between the present detectors and the original preamplifier. This should result in a substantial improvement in MSDS performance for these channels. The modification can best be done at JSC and the authors would be glad to advise on this.

2
BACKGROUND

The present sky irradiance measurement apparatus of the MSDS essentially consists of a transmissive opal glass diffuser located in the skin at the top of the aircraft fuselage. The opal glass, which is viewed by the scanner through a 24-in. focal length, 6-in.-diameter quartz lens, fills 6 in. of the 9-in.-diameter scanner field of view. Although opal glass is perhaps the closest one might come to an ideal transmissive Lambertian diffuser (for the visible spectrum), such a diffuser is not ideal for this particular application. The cosine dependence of the power transmitted through the opal glass results from the fact that the projected sensor collecting area is dependent on the solar zenith angle. This cosine dependence leads to variations in sky irradiance measurements as aircraft attitude and solar elevation angle change. Variations of ±10% in signal with $\pm 5^{\circ}$ roll or pitch for a sun zenith angle of 50° can be expected.

We propose a diffusing apparatus (made independent of this cosine variation) that would produce data of much greater value for determination of atmospheric and illumination conditions. Also, direct illumination from the sun should be blocked periodically (mechanically, e.g., by a rotating arm above the sky irradiance sensing device) in order to permit the apparatus to measure not only total sky illumination but also scattered illumination from the sky (with the sun blocked).

Preliminary consideration of such an apparatus with respect to practicability, fabrication, information accuracy, and operational usage has led to the list of goals shown in Table 1. Sections 3 and 4 describe the various designs considered to meet these goals.

TABLE 1. LIST OF DESIGN GOALS

Performance Parameter	Goal	Acceptable Minimum
% diffuse reflector on ground, equivalent to throughput for sun at zenith (extrapolated if necessary)	>5%	> 2% . .
Range of incident angles (from zenith) comprising "clear" field of view	10^{o}-70^{o}	10^{o}-60^{o}
% variation in throughput within "clear" field of view	<±5% (10^{o}-70^{o})	<±10% (10^{o}-60^{o})
% variation in throughput for ±5^{o} roll of aircraft (within "clear" field of view)	<±1% (15^{o}-65^{o})	<±3% (15^{o}-55^{o})
% variation in throughput for scan angle variation about "zenith"	<±5% ±0.035 radian	<±20% ±0.017 radian
% view of sky when the sun is blocked (mechanically)	>50%	> 20%
Ratio of background signal in a scatterless atmosphere with the sun blocked (mechanically) to signal from the sun alone (sun unblocked)	<2%	<10%
% of scanner field of view utilized	100%	> 25%
Spectral range of sensitivity	0.4μm-2.0μm	0.4μm-0.8μm
Diameter of apparatus at aircraft skin	<12 in.	<24 in.
Maximum projection of apparatus into airstream	0 in.	<12 in.

3
SKY REFERENCE SENSOR

Two different approaches were considered in an effort to minimize the angular dependence of the sky reference sensor. One system was designed around a hyperbolic mirror and a reflective approach, while another utilized a fish-eye lens in a refractive approach. Both systems were designed, built, and tested according to the same criteria to insure proper comparison of their performance characteristics. For each, the theory behind the design and the results of the testing are explained below.

3.1 HYPERBOLIC MIRROR SKY REFERENCE

3.1.1 DESIGN CONSIDERATIONS

Measuring the illumination received at a point independently of the illumination's angle of incidence requires an apparatus which receives the radiation converging toward this point and reflects, refracts, and/or scatters the light into the field of view of the scanner. Use of a hyperboloidal or ellipsoidal mirror can cause the light converging toward one focus of the mirror to be reflected toward the other focus and from there to be scattered into the scanner field of view. In order to have a finite and constant throughput, the first focal point must be expanded into an irregular-shaped area whose receiving cross-section is more or less constant for all illumination angles of interest. This may be done by placing a suitable receiving area, such as a flat reflective diffusing disk, at the other focal point of the mirror.

Examination of the formulas for hyperboloidal and ellipsoidal mirrors reveals that such an arrangement is possible. If we let (see Fig. 1)

h = distance between foci of mirror

M = major axis of ellipsoid, or minimum distance between the two sheets of a hyperboloid

Θ_i = angle of incidence for incoming radiation on mirror measured from zenith

h/M = mirror shape

Θ_e = angle of incidence for reflected radiation incident on diffuser measured from nadir

$R_i(\Theta_i)$ = distance from first focal point to mirror surface

$R_e(\Theta_e)$ = distance from second focal point to mirror surface

$A_i(\Theta_i)$ = effective receiving cross-sectional area for collimated incoming radiation

A_e = area of disk's surface viewed by scanner

we obtain the formulas given below.

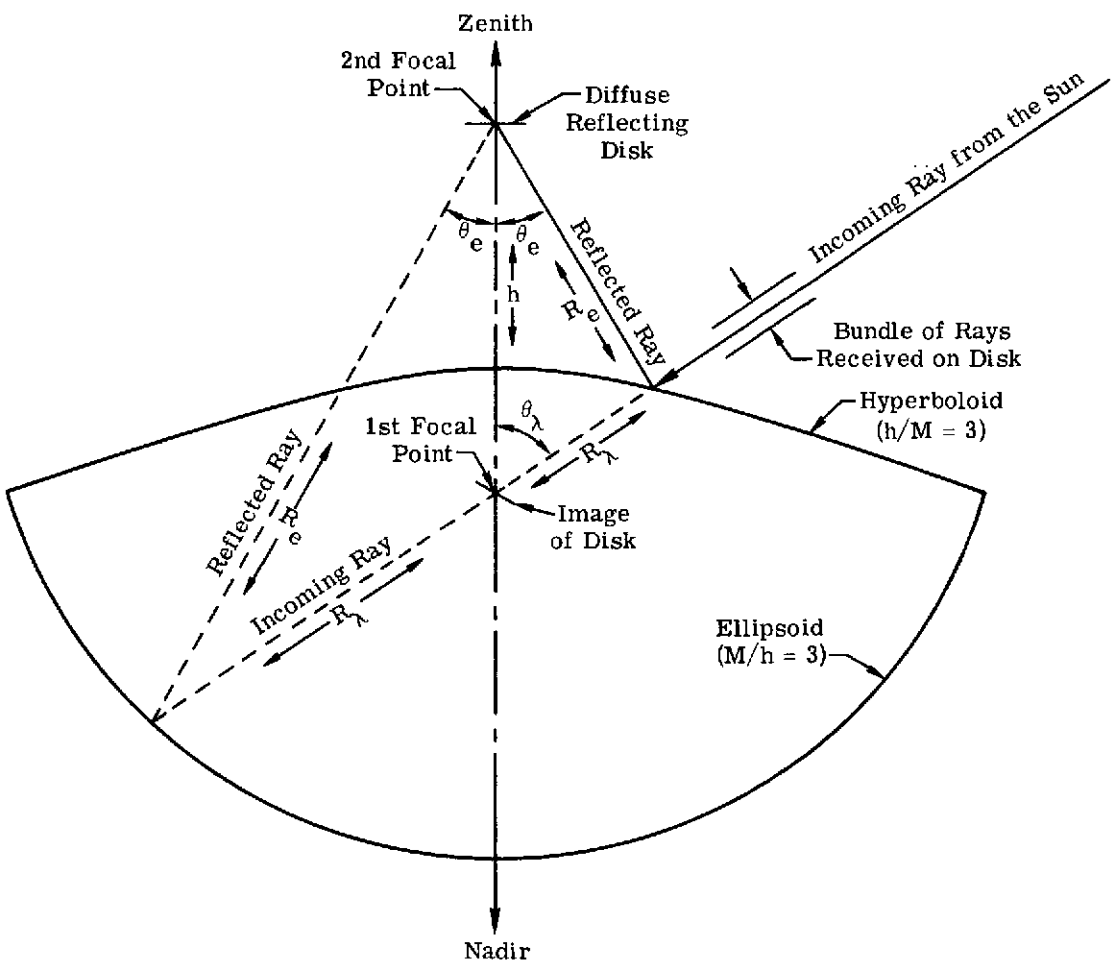

FIGURE 1. DEFINITION OF TERMS USED IN MIRROR SYSTEM ANALYSIS. Both the hyperboloid and ellipsoid reflecting surfaces are depicted to show the optical path of each and the similarities between them.

Definition of a hyperbola or ellipse:

$$R_e - R_i = M (R_i > 0 \text{ for hyperbola, } <0 \text{ for ellipse}) \tag{1}$$

Formula for a hyperbola or ellipse in polar coordinates about the first focal point:

$$R_i = \frac{\frac{h}{2}\left(\frac{h}{M} - \frac{M}{h}\right)}{\frac{h}{M}\cos\Theta_i + 1} \left(\frac{h}{M} > 1 \text{ for hyperbola, } <1 \text{ for ellipse}\right) \tag{2}$$

About the second focal point:

$$R_e = \frac{\frac{h}{2}\left(\frac{h}{M} - \frac{M}{h}\right)}{\frac{h}{M}\cos\Theta_e - 1} \tag{3}$$

Relative throughput of the device:

$$\frac{A_i}{A_e} \simeq \left(\frac{R_i}{R_e}\right)^2 \cos\Theta_e \tag{4}$$

$$= \text{relative minimum when } \Theta_e = 0$$

$$= \text{maximum when } \cos\Theta_e = \frac{1}{6}\left(\frac{h}{M} + \frac{M}{h}\right)$$

Figure 1 shows a typical ray trace for an ellipsoid or hyperboloid reflective surface. Envision the scanner viewing the diffusely reflecting disk through a small hole in the center of the reflecting surface. Both reflective surfaces are depicted in Fig. 1 to show the similarities between them. An actual unit would incorporate one or the other. Equation (4) is approximate because the distortion of the diffuser image caused by the curvature of the mirror is not considered. However, this omission causes negligible error. If Eq. (4) is written as a function of Θ_e by substituting for R_i using Eq. (1) and then for R_e using Eq. (3), it becomes apparent that for any hyperbola with $h/M = K$, an ellipse with $M/h = K$ yields identical results for Eq. (4). For a non-Lambertian diffusing disk, the right-hand side of Eq. (4) must be multiplied by $\rho'(\Theta_e)$, the bi-directional reflectance characteristic of the diffusing material chosen, to determine the actual throughput characteristics of the mirror-diffuser system implemented. Figure 2 plots Eq. (4) (throughout) as a function of Θ_e for various h/M ratios for a hyperbolic mirror (assuming a Lambertian diffuser is used); the same plot applies to an elliptic mirror if h/M is replaced by M/h.

Since flame-sprayed aluminum is durable and highly reflective and has nearly constant bi-directional reflectance characteristics for a wide range of wavelengths, it would appear to be a good choice for a reflective diffusing material. If the bi-directional reflectance of flame-sprayed aluminum, $\rho'(\Theta_e)$, is included in Eq. (4), then for incident angles (Θ_i) between 10^o and

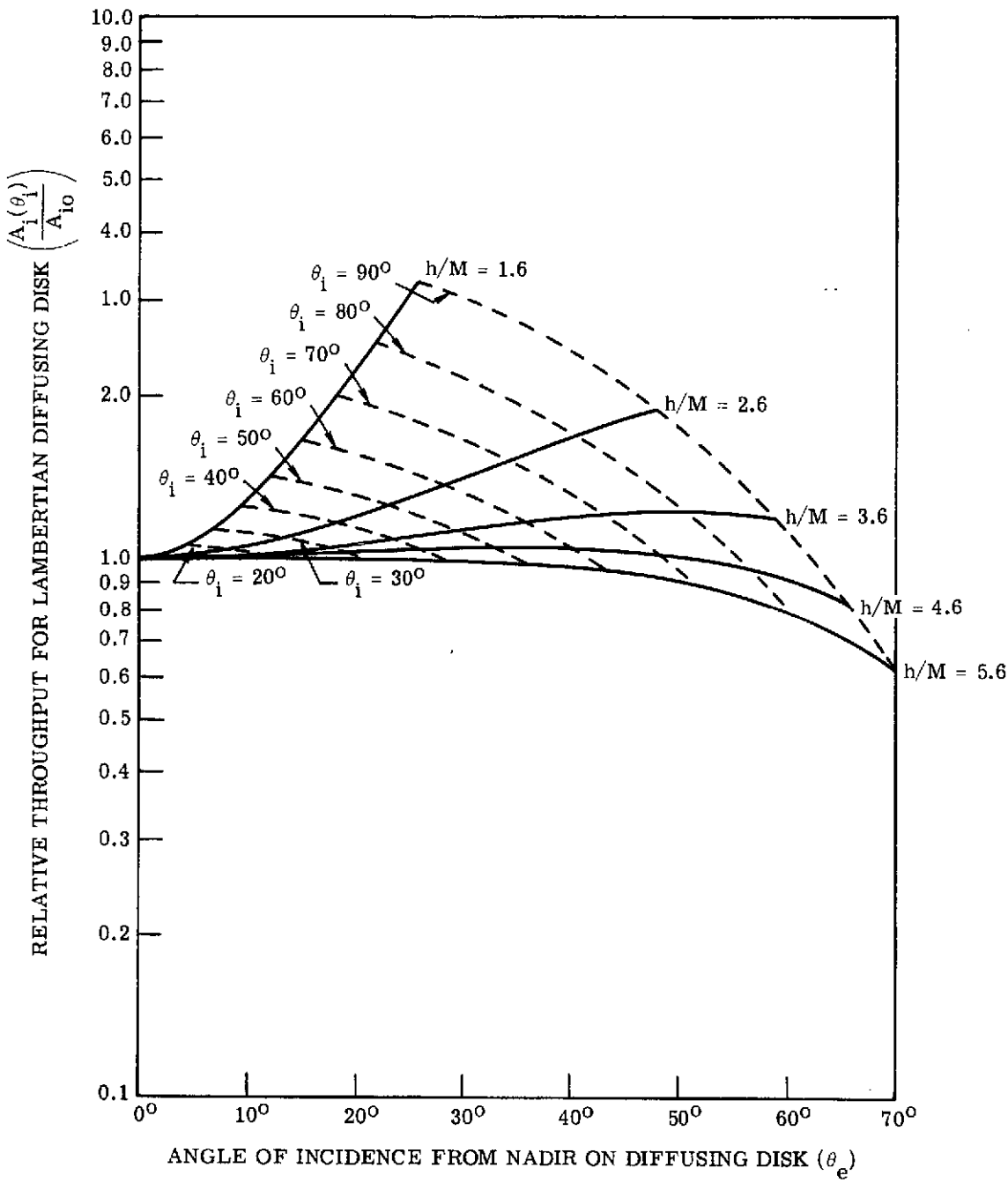

FIGURE 2. RELATIVE MIRROR SYSTEM THROUGHPUT VERSUS RESULTANT ANGLE OF INCIDENCE FOR LAMBERTIAN DIFFUSING DISK WITH VARIOUS MIRROR GEOMETRIES h/M

70^{o}, a value of h/M = 3.6 (for a hyperbolic mirror) is near the optimum for throughput independence of the angle of incidence. This value compensates for the non-Lambertian reflectance characteristics of the flame sprayed aluminum. Thus the optimum shape for the mirror specified by h/M (eccentricity) is determined by the choice of diffusing material.

The optimum size (scaling) of the mirror is determined by other considerations which are discussed in Section 3.1.3.

3.1.2 TESTING THE DESIGN

To test the mirror-diffuser design, a 12-in.-diameter hyperbolic mirror with a 75^{o} field of view (Θ_i between 0^{o} and 75^{o}) and h/M = 3.6 was turned on a lathe and hand-polished. This mirror was set up in a lab and tested in the configuration shown in Figs. 3, 4, and 5. The mirror was illuminated by a 200-watt quartz-iodine lamp (to simulate the sun) which could be rotated about the first focal point of the mirror at a distance of 18 in. (see Fig. 4). To receive the signal from the mirror-diffuser system, a simulated scanner was constructed using a 0.02-in.-diameter silicon detector located at the focal point of a 9-3/16-in. focal length, 4-1/8-in.-diameter lens (see Fig. 5). The lens of this simulated scanner was then imaged on the 2-in.-diameter flame-sprayed aluminum diffusing disk, through a 0.6-in. hole (image plane of the detector) in the center of the hyperbolic mirror, by using a 16.7-in. focal length, 11-in.-diameter lens (see Figs. 3 and 4). The simulated scanner and lens behind the mirror were positioned so that the center of the hole in the mirror was located at the focal point of the 16.7-in. focal length lens. The system was aligned by using a 0.63 μm laser. Many of these components were used because they were available and not because we wanted to test a specific layout for a particular system. The goal was to show correlation between theoretical analysis and experimental measurements.

At first the hyperbolic mirror was not highly polished. This led to the immediate discovery that any scratches on the mirror surface, particularly parallel or concentric scratches, caused intolerable scattering. After the mirror was more carefully polished, however, no scratches were apparent to the eye. It was noted, though, that near the outer edge of the mirror and near the edge of the hole in the center of the mirror, the shape of the mirror had been altered slightly by the polishing process. The throughput measured for this mirror as a function of the angle of incidence of the light from the lamp is plotted in Fig. 6 together with the theoretical throughput. Note that the throughput is very uniform except when the outside edge of the mirror and the edge of the hole in the center begin to obscure the field of view of the mirror-diffuser apparatus. The slight increase in measured throughput which occurs at an incident angle of $\approx 20^{o}$ may be caused by the fact that the flame-sprayed aluminum disk has somewhat specular reflectance characteristics. This probably is due to insufficient depth of the flame-sprayed coating or to wearing of the surface.

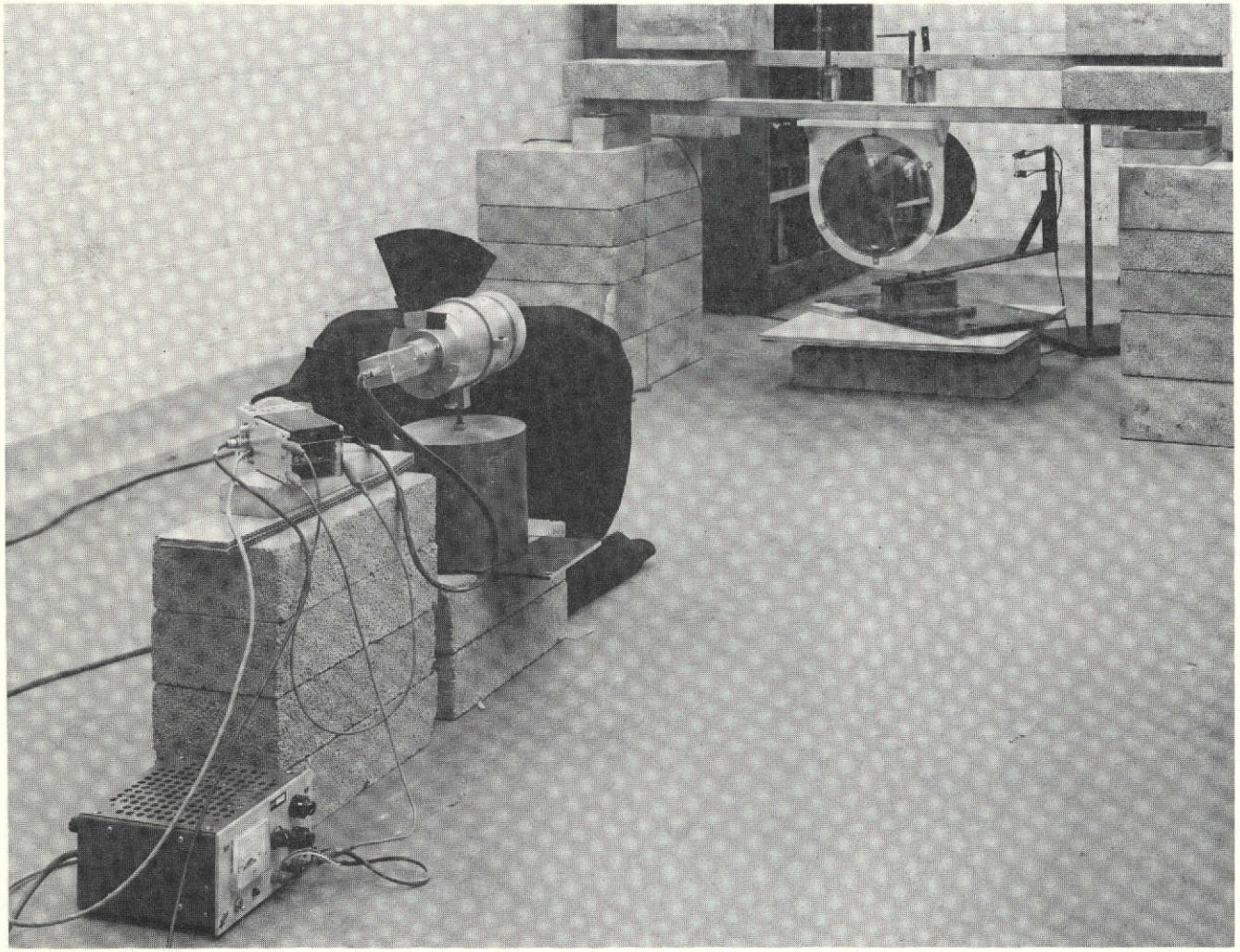

FIGURE 3. REFLECTIVE TEST CONFIGURATION (OVERALL VIEW)

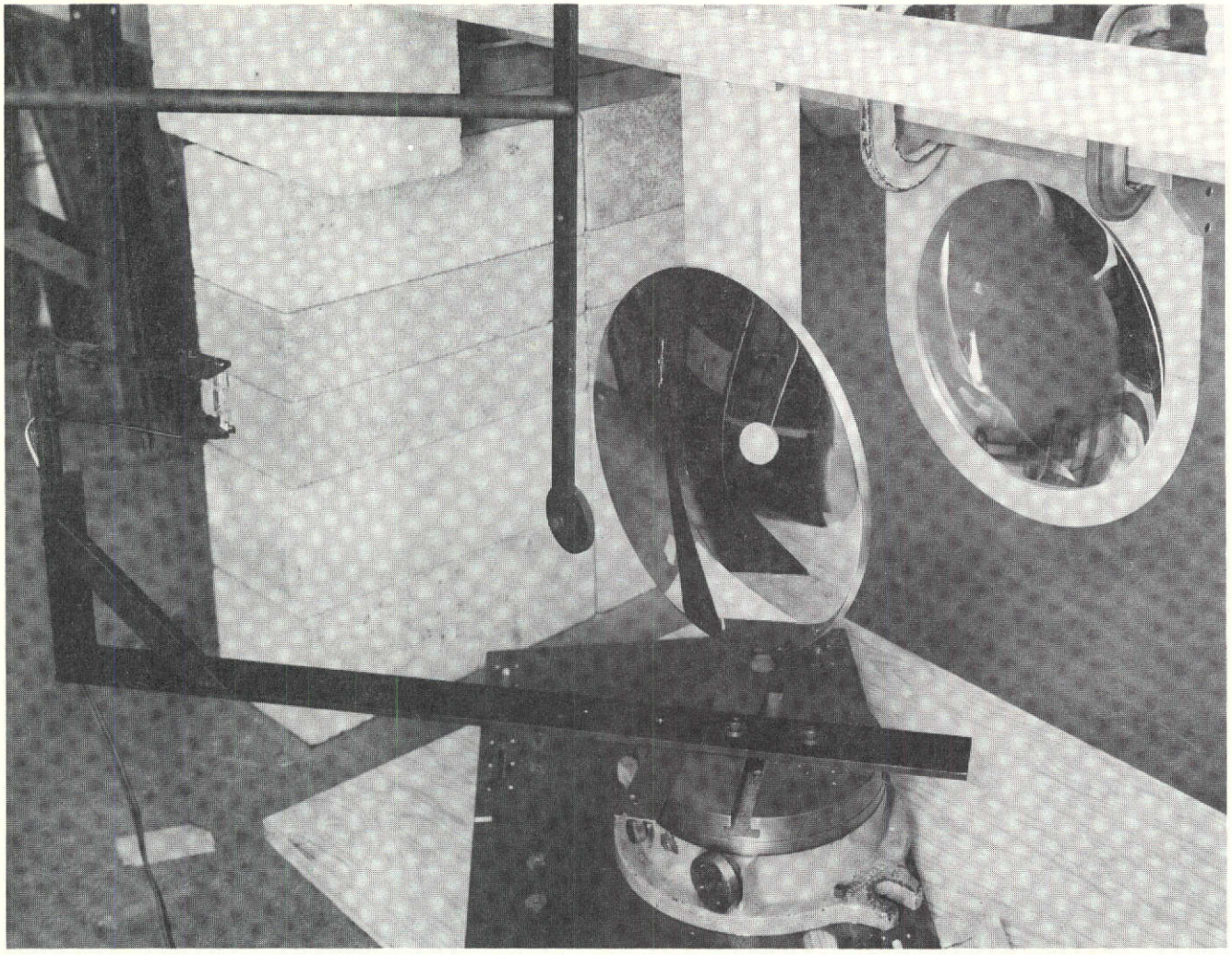

FIGURE 4. REFLECTIVE TEST CONFIGURATION (SIMULATED SUN, DIFFUSER, MIRROR AND LENS)

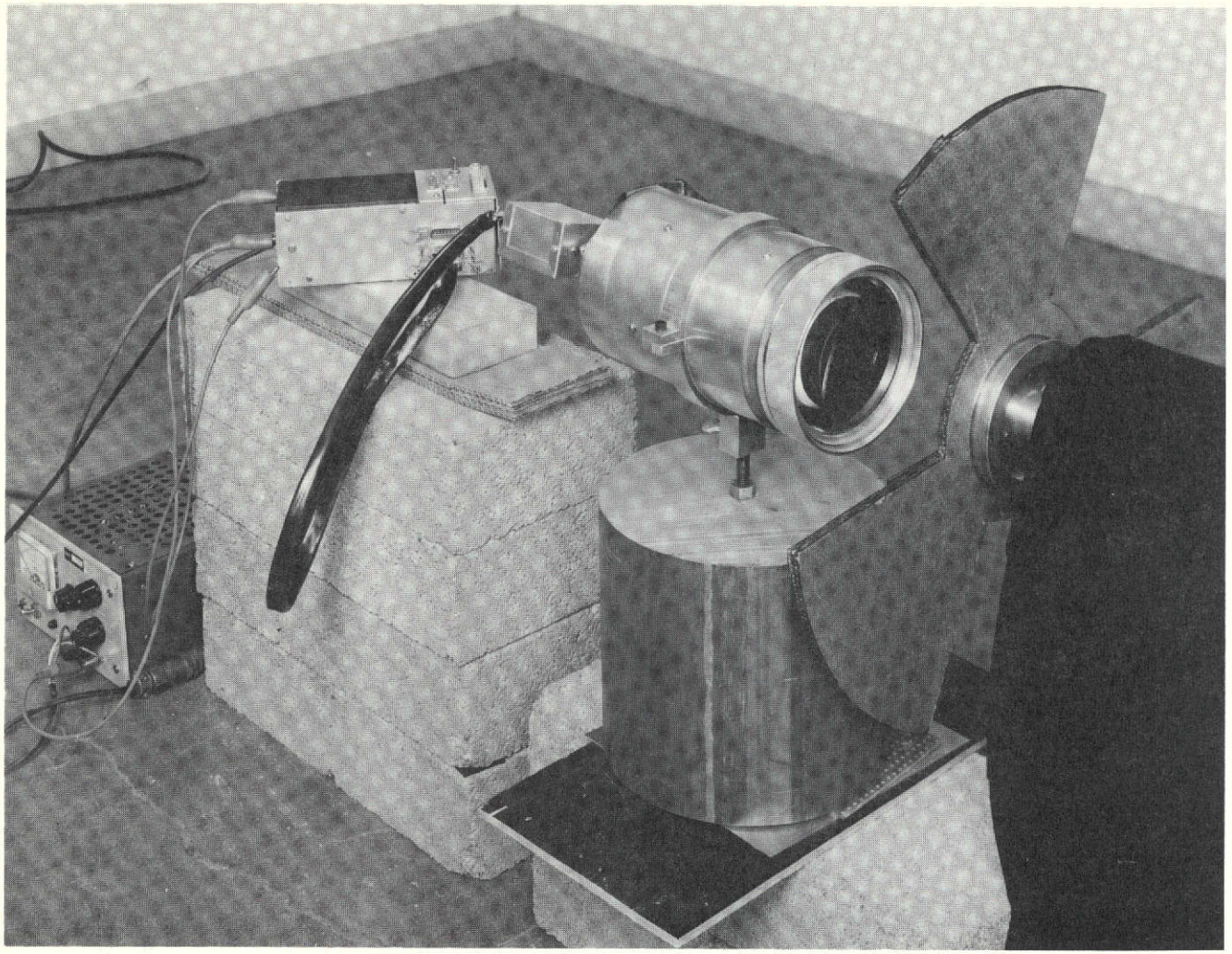

FIGURE 5. REFLECTIVE TEST CONFIGURATION (CHOPPER AND SCANNER SIMULATOR)

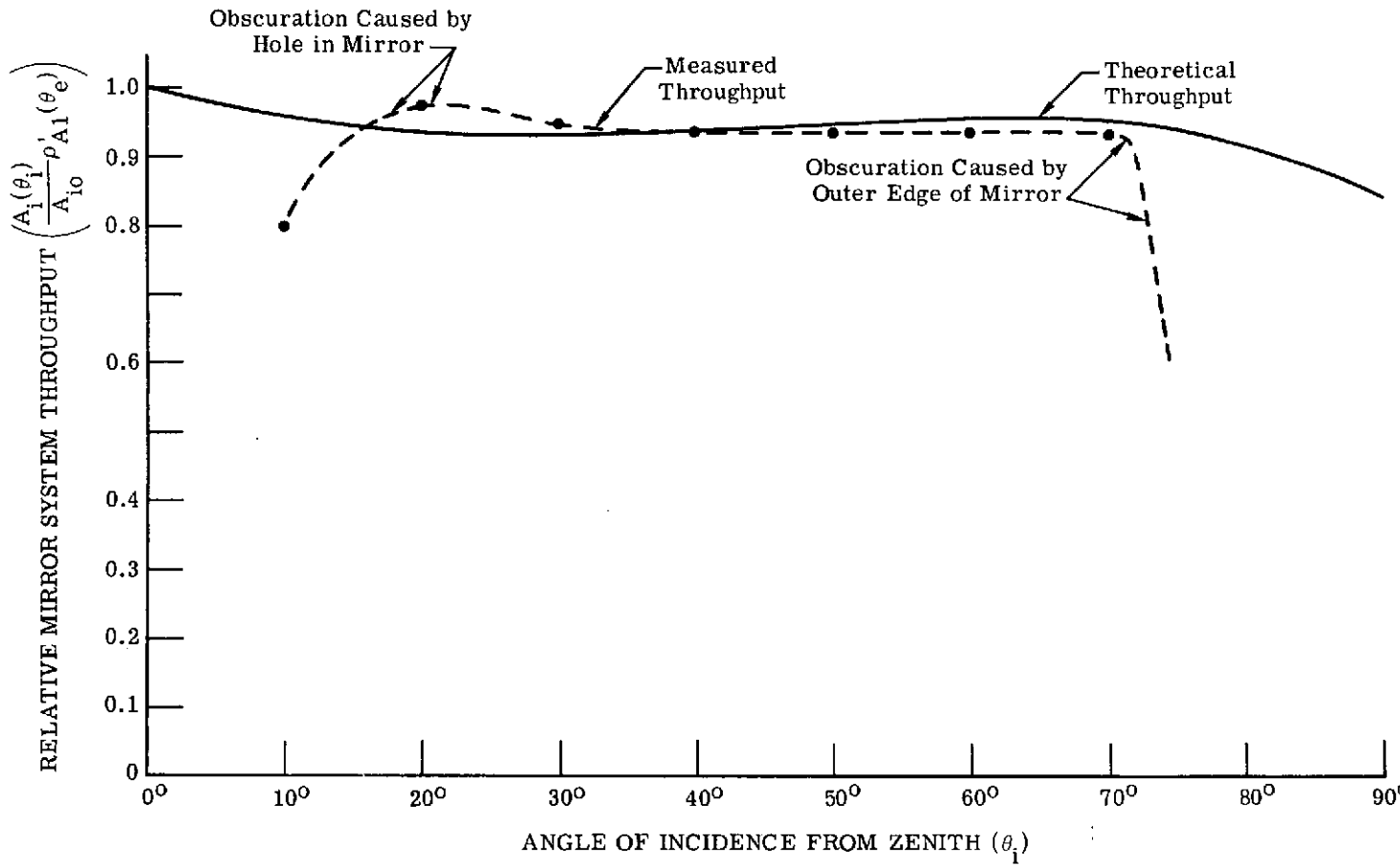

FIGURE 6. RELATIVE MIRROR SYSTEM THROUGHPUT VERSUS ANGLE OF INCIDENCE FROM ZENITH USING FLAME-SPRAYED ALUMINUM AND HYPERBOLIC MIRROR WITH h/M = 3.6

Measurements also indicated that the throughput of the mirror-diffuser system was independent of scan angle between 0^{o} and $\pm 1.0^{o}$. This was the range predicted when the size of the hole in the mirror, the detector size, and the aberrations of the lenses were considered. In addition, the contribution to the throughput caused by scattering resulting from imperfections in the mirror was measured and found to be on the order of 1 percent. In general, the mirror-diffuser system performed according to the predictions of its design theory.

3.1.3 IMPLEMENTING THE DESIGN

The first problem encountered in implementing the mirror-diffuser system is the obscuration of the system's field of view for incident angles near the zenith caused by the diffusing disk and by the hole in the mirror (for viewing the disk). If we let

α_{-} = amount of obscuration of field of view near zenith

$\pm\alpha'$ = duration (angle) of scan over which full throughput is desired

2∂ = resolution of scanner (~0.022 radians)

$d_m(\Theta_i)$ = diameter of mirror corresponding to given angle of incidence (Θ_i) measured from zenith

d_b = diameter of rotating scan mirror utilized (remainder to be blocked out by a baffle)

K_1 = constant

and if we consider the geometry of the optical rays, we may write

$$\alpha_{-} \simeq K_1 \sqrt{\frac{d_b}{d_m}(\alpha' + \partial)} \tag{5}$$

This relation is plotted in Fig. 7. We have assumed d_b = 6 in. (diameter of rotating scan mirror = 9 in.) and $\alpha' = 1.2^{o}$ (16 reselms plus 2 reselms extra to provide a tolerance for misalignment of the mirror-diffuser system). Note that a very large mirror (~40 in. in diameter) would be needed to provide a clear field of view from 10^{o} to 70^{o} angle of incidence. An unobstructed FOV at $\Theta_i = 70^{o}$ required that the outer edge of the mirror correspond to $\Theta_i = 75^{o}$ as a result of the width of the mirror's effective receiving aperture (see Figs. 7 and 8). To obtain Eq. (5), some assumptions were made regarding both the distance (D) behind the surface of the hyperbolic mirror at which the baffle which limits the utilized diameter of the rotating scan mirror is placed and the focal length (f) of the lens used to image this baffle on the diffusing disk. Namely,

$$f = \sqrt{\frac{h - M}{2}\frac{d_b}{2(\alpha' + \partial)}} \text{(optimum focal length of imaging lens)} \tag{6}$$

$$D = \left\{ \left(\frac{2f}{h + M} + 1 \right)^2 - 1 \right\} \frac{h + M}{2} \text{(optimum location of baffle behind the mirror)} \tag{7}$$

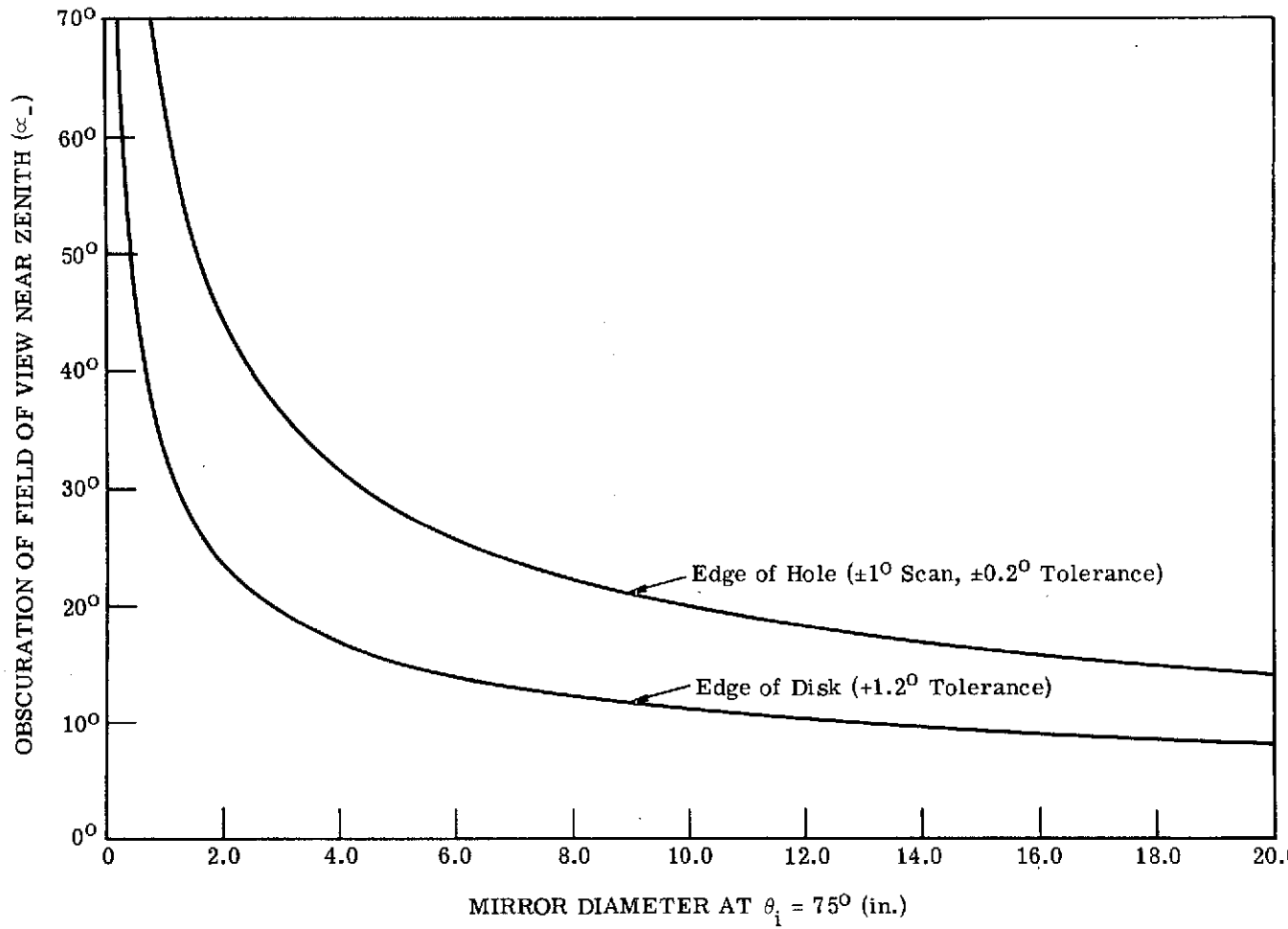

FIGURE 7. OBSCURATION OF FIELD OF VIEW NEAR ZENITH (α) VERSUS SIZE OF HYPERBOLIC MIRROR (h/M = 3.6) USING 6 INCHES OF SCAN-MIRROR DIAMETER

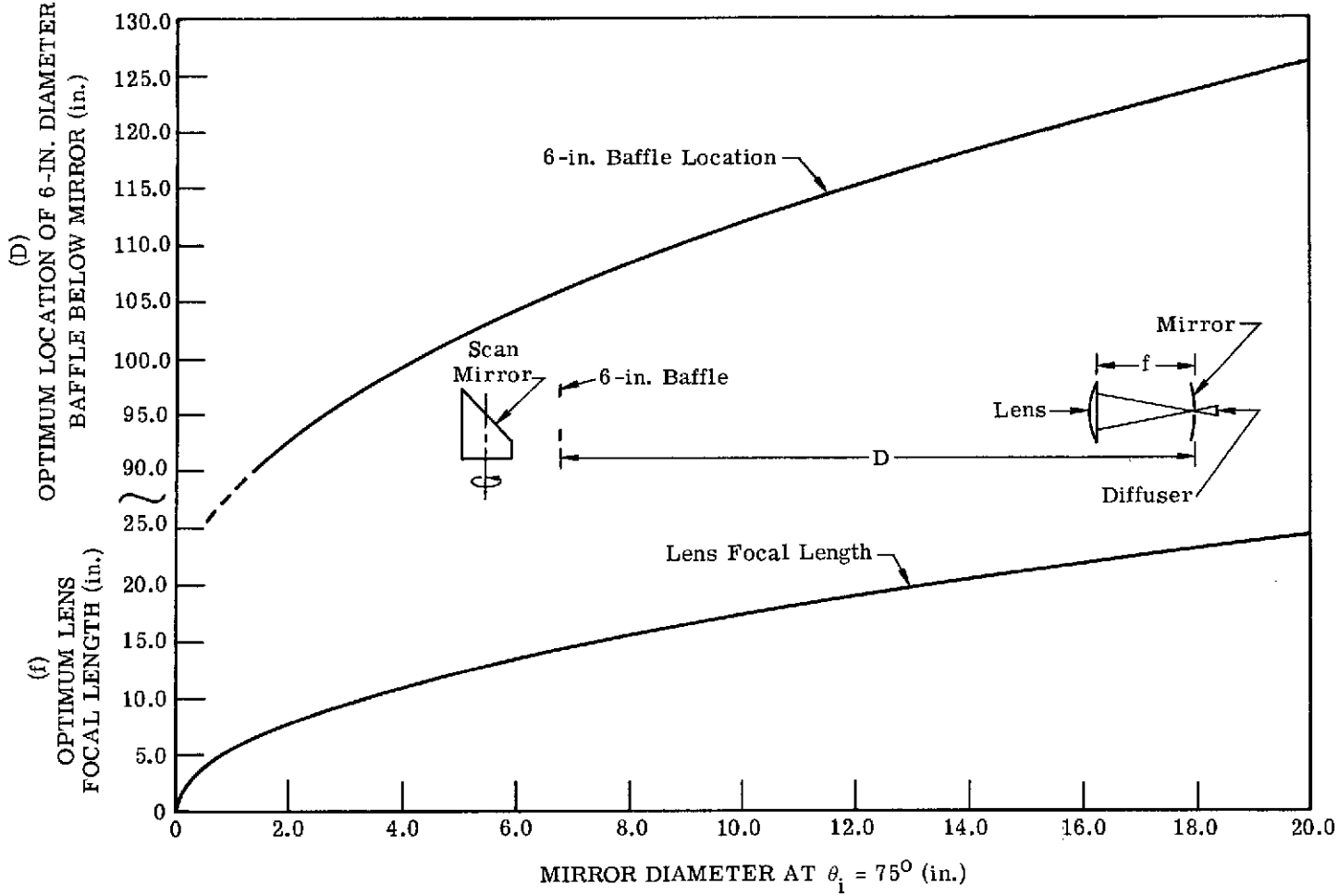

FIGURE 8. 6-INCH BAFFLE LOCATION AND LENS FOCAL LENGTH VERSUS SIZE OF HYPERBOLIC MIRROR (h/M = 3.6)

where

$\frac{h - M}{2}$ = distance from center of mirror to first focal point, and

$\frac{h + M}{2}$ = distance from center of mirror to second focal point

Equations (6) and (7) are plotted in Fig. 8.

A second problem encountered in implementing the mirror-diffuser system was that of blocking the reflected light from the surface of the ground or from the skin of the aircraft (which would tend to illuminate the diffusing disk directly). If we imagine a circular shield surrounding the hyperbolic mirror and let

ρ_s = reflectance of shield (e.g., 4%)

ρ_G = average reflectance of ground (e.g., 20%)

Θ_+ = angle from nadir about diffusing disk blocked by shield

Θ_- = angle from nadir about diffusing disk over which disk sees reflection of sky (not shielding) in mirror

ϵ = scattering contribution from imperfections in mirror (~2%)

S_s = minimum throughput from sun with scatterless atmosphere and perfect shielding against unwanted reflections

S_B = throughput from background (mounted reflections)

we have

$$\frac{S_B}{S_s} \simeq \left\{ (\rho_G - \rho_s) \cos^2 \Theta_+ + \rho_s \cos^2 \Theta_- \right\} \frac{A_e}{A_{io}} + \epsilon \qquad (8)$$

In general, this formula implies that $S_B/S_s \sim 10\%$ for $\Theta_+ = 80^\circ$ or $S_B/S_s \sim 15\%$ for $\Theta_+ = 70^\circ$ (assuming that the field of view of the mirror-diffuser system goes out to 70° from zenith). An idea of the interrelations among mirror size and field of view and the amount of shielding and its size is given in Fig. 9. Only a 16-in.-diameter shield is required for 60° FOV with a 70° shield, but more than a 31-in.-diameter shield is required for a 70° FOV with an 80° shield.

3.1.4 PRACTICAL LIMITATIONS

Note that, in general, performance of the mirror-diffuser system improves in all respects as the size of the apparatus is increased; however, when fabrication and installation of the design are considered, a small apparatus is desirable. Figures 10 and 11 illustrate three basic approaches to implementation of the mirror-diffuser design, each drawn 1/5 actual size. Each is a compromise between different performance characteristics of the system.

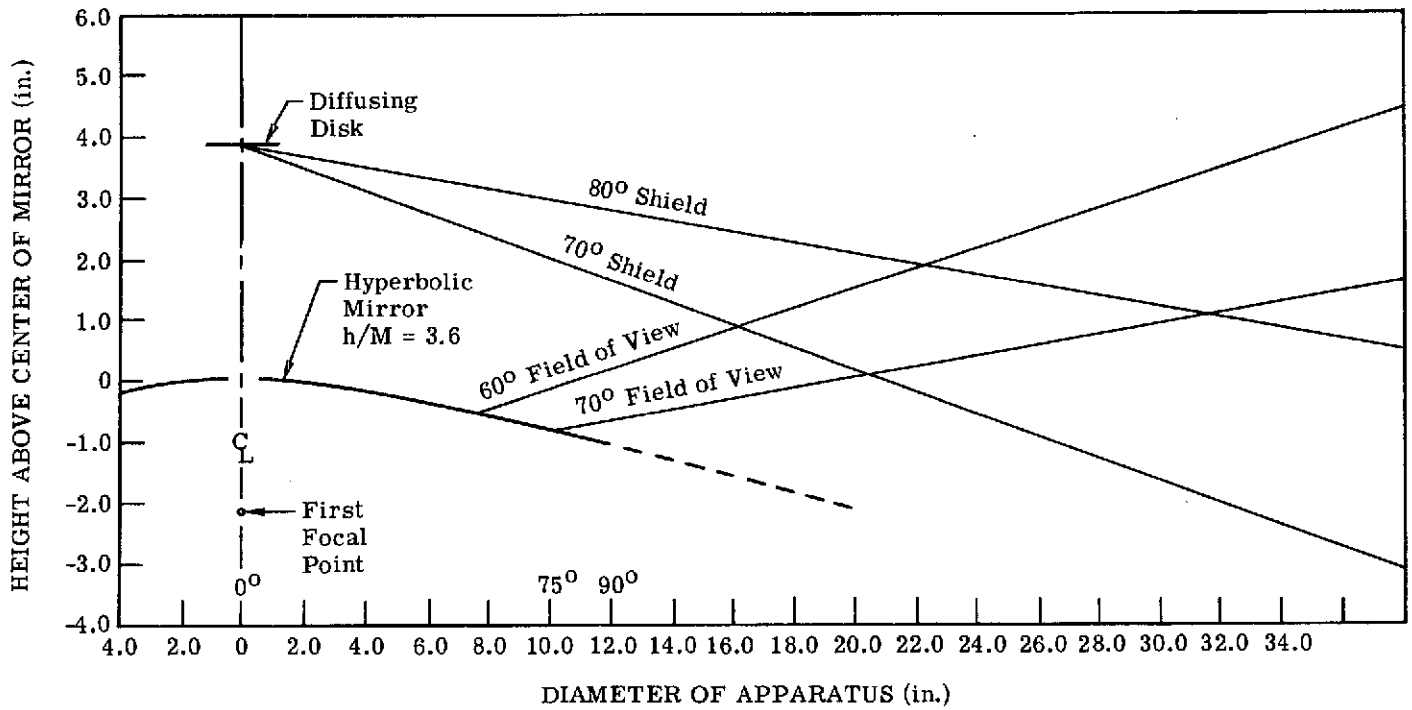

FIGURE 9. BACKGROUND SHIELDING VERSUS FIELD OF VIEW FOR HYPERBOLIC MIRROR

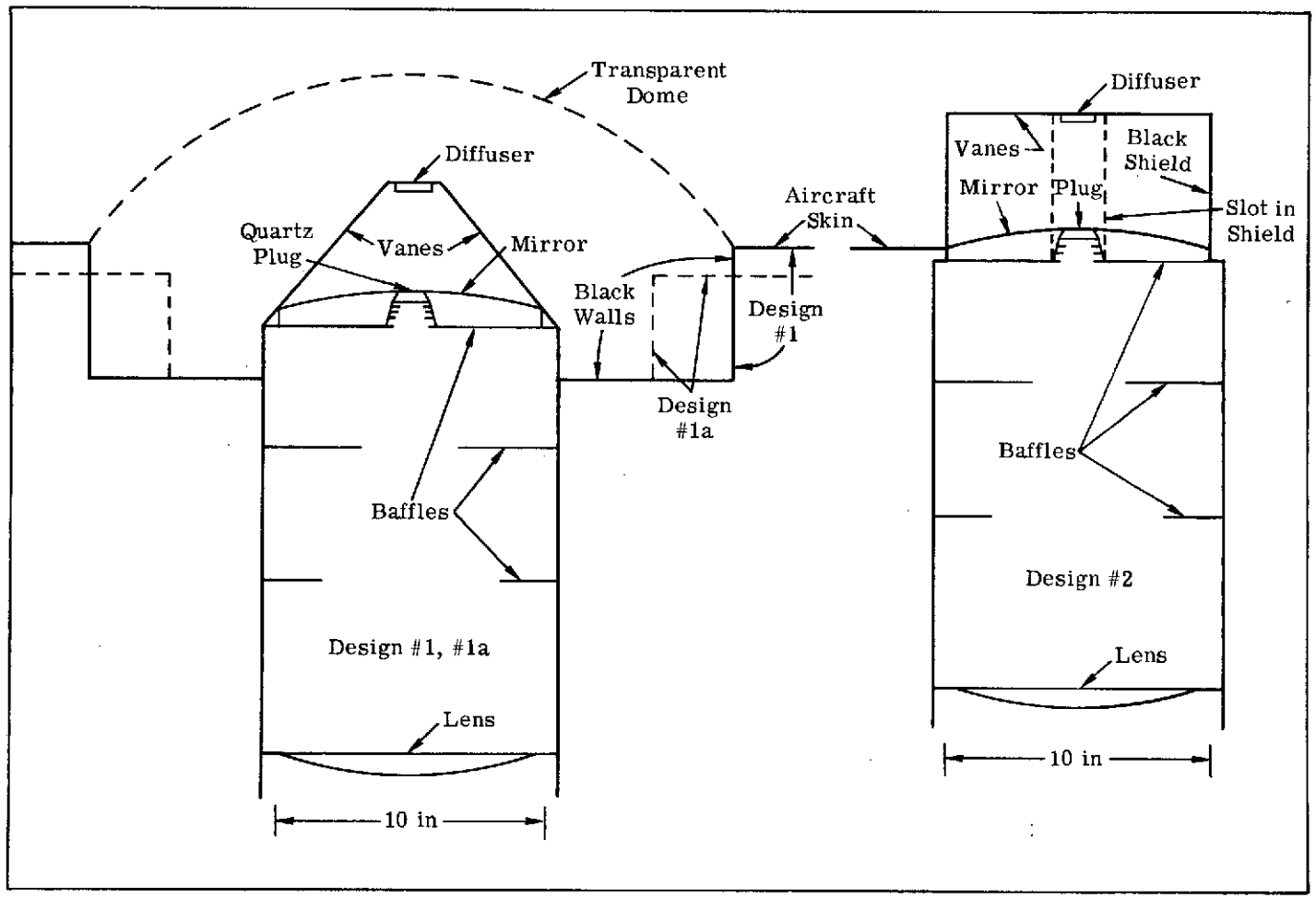

FIGURE 10. TWO BASIC DESIGN CONCEPTS

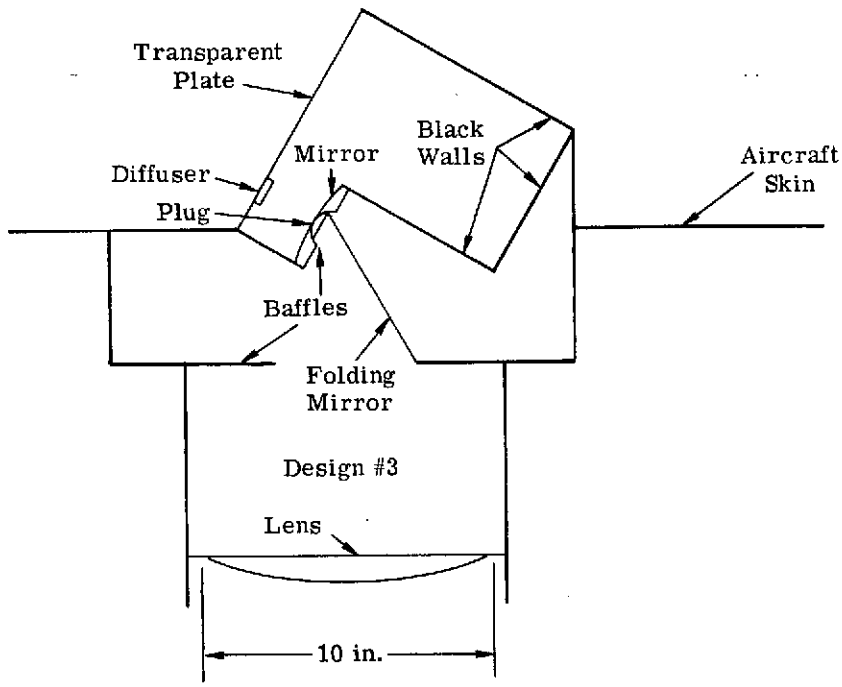

FIGURE 11. A THIRD BASIC DESIGN CONCEPT

Design #1 is a rather straightforward one based on the discussion in this report. The diameter of the shield around the mirror is 24 in., while the mirror itself is 10 in. in diameter with a field of view out to 70^{o} from zenith. Here, field of view near the zenith has been sacrificed—it is obscured for the first 20^{o}. If the roll and pitch of the aircraft are limited to $\pm 5^{o}$, the sun would be in the FOV of the instrument at all times for latitudes north of Houston, Texas.

One might also consider design #1A (similar to design #1 but with less shielding), in which the diameter of the shield would be reduced to 18 in. and the diffuser would protrude 1 in. farther into the airstream.

Note that designs #1 and #1A could be covered with a transparent dome (e.g., plexiglass or quartz) to protect them from weather and the airstream, although any scratches on the dome would increase scattered radiation into the instrument. In both these designs, the vanes and the diffuser (and possibly the mirror as well) could be rotated to block the sun periodically.

Another modification of design #1, design #2, has a slotted "stovepipe" shield and vanes across the top to support the diffuser. Transparent material could be used to cover the top of the shield and the slots in the sides. The vanes and the slotted shield together would assure that periodically the sun would either be blocked or visible depending on the rotation angle of the shield, vanes, and diffuser assembly. For sun angles of incidence between 36^{o} and 44^{o}, data from this apparatus would be usable, but somewhat confusing as a result of the effects of the shield's edge. For sun angles of incidence greater than 36^{o}, sun-glint from water or from other shiny areas on the ground would be received by the apparatus in such a way as to interfere with its performance.

Design #3 provides a fuller field of view near the zenith than does any of the other designs but at the expense of having a large rotating optical apparatus (on the order of 16 in. in diameter). This design would scan the sky as it rotated and would periodically block the sun (no vanes are needed). The mirror shown is 3.1 in. in diameter and would permit 75^{o} angle of incidence.

For all these designs, for that part of the device which is rotating the frequency would be about 1 revolution every 6 sec. This will mean that the sun will be blocked out during about half of the total scanlines: that is, 15 out of every 30 scanlines at the lowest V/H and 150 out of every 300 at the highest V/H.

Characteristics of these various designs are summarized in Table 2.

We should note that the distance from the top of the skin of the C-130 aircraft to the axis of rotation of the scan mirror is only 118 in.; hence, designs #1 and #3 would have to have the

TABLE 2. DESIGN REQUIREMENTS FOR REFLECTIVE SYSTEM

Performance Parameter	Goal	Acceptable Minimum	Present Design Opal Glass	Design #1, #1A	Design #2	Design #3
% diffuse reflector on ground, equivalent to throughput for sun at zenith (extrapolated if necessary)	>5%	>2%	50%	16%	16%	16%
Range of incident angles (from zenith) comprising "clear" field of view	10^{o}-70^{o}	10^{o}-60^{o}	0^{o}-85^{o}	20^{o}-70^{o}	20^{o}-70^{o}	9.5-75^{o}
% variation in throughput within "clear" field of view	<±5% (10^{o}-70^{o})	<±10% (10^{o}-60^{o})	<±33% (10^{o}-60^{o})	±0.2% (20^{o}-70^{o})	±1.2% (20^{o}-70^{o})	±1.2% (9.5-75^{o})
% variation in throughput for ±5^{o} roll of aircraft (within "clear" field of view)	<±1% (15^{o}-65^{o})	<±3% (15^{o}-55^{o})	<±15% (0^{o}-60^{o})	<±0.5% (25^{o}-65^{o})	<0.5% (25^{o}-65^{o})	<±0.5% (15^{o}-70^{o})
% variation in throughput for scan angle variation about "zenith"	<±5% ±0.035 radian	<±20% ±0.017 radian	<±5% ±0.17 radian	<±1% ±0.017 radian	<±1% ±0.017 radian	<±1% ±0.017 radian
% view of sky when the sun is blocked (mechanically)	>50%	>20%	does not apply	52%	18%	27%
Ratio of background signal in a scatterless atmosphere with the sun blocked (mechanically) to signal from the sun alone (sun unblocked)	<2%	<10%	does not apply	11% (#1) 15% (#1A)	16%	12%
% of scanner field of view utilized	100%	>25%	42%	42%	42%	42%
Spectral range of sensitivity	0.4μm-2.0μm	0.4μm-0.8μm	0.35μm-0.8μm	0.3μm-4.0μm	0.3μm-4.0μm	0.3μm-4.0μm
Diameter of apparatus at aircraft skin	<12 in.	<24 in.	≅2 in.	20 in. (#1) 15 in. (#1A)	8.4 in.	13.3 in.
Maximum projection of apparatus into airstream	0 in.	<12 in.	0	2.1 in. (#1) 2.9 in. (#1A)	4.2 in.	6.3 in.

distance from the hyperbolic mirror to the 6-in. baffle (D in Fig. 8) reduced to ~100 in. instead of the 111.75-in. optimum distance. The focal length of the large imaging lens would also have to be reduced from 17.24 in. to 16.14 in. The effect of these changes on performance would be negligible, however. The obstruction near the zenith for incoming light would be increased by only 0.044^{o} for the edge of the hole in the mirror, and by only 0.68^{o} for the edge of the diffusing disk (see Fig. 7).

3.2 FISH-EYE LENS SKY REFERENCE

3.2.1 DESIGN CONSIDERATIONS

As with the mirror system, the primary interest in developing a sky reference apparatus utilizing a refractive lens was to minimize variations in throughput with source angle and receiver angle. Unfortunately, this part of the study did not lend itself to a detailed theoretical analysis since the fish-eye lens used in the apparatus was foreign made and could not be analyzed without additional information. As a result, most of the designs discussed below were selected by empirical methods. Many minor changes were made in the course of testing to improve performance, some of which will not be noted in detail.

The particular lens used for this study was a Nikkor 8mm f/2.8 fish-eye lens normally used on 35mm cameras. Since actual images were not important in any of these sky references, the two negative lenses which provide the wide field of view were removed from the lens body and adapted for use on the sky references. The lenses were tested in both a double and a single configuration. The first lens was considerably larger than the second; hence, the increased throughput from utilizing the larger lens singularly was considered a worthwhile study.

In designing an apparatus to view the energy received by the fish-eye lens, considerably more study was required than just buying the lens since variations with receiver angle (which can occur with the rotation of the scan mirror as it views the sky reference) had to be minimized while, at the same, throughput had to be maximized. We eventually experimented with two different approaches. One, which utilized an integrating sphere, was fabricated and tested; a second, based upon a relatively simple opal-glass concept, was also studied. A discussion of these two approaches follows.

3.2.2 FISH-EYE LENS/INTEGRATING SPHERE DESIGN

A major modification had to be made to the ideal integrating-sphere concept to allow for potential installation in an aircraft. In normal use, the integrating sphere has an entrance port on top and an exit port on the side. Without using mirrors, however, this is totally impractical for viewing with the MSDS scanner. The modification made to the ideal device included the inserting of a baffle in the center of the sphere (to block direct rays) and placing the

exit port directly opposite the entrance port. This allowed the integrating sphere to be located above the scanner in a direct line with the opening in the skin of the aircraft.

Shown in Fig. 12 is a cross section of the integrating sphere/fish-eye lens assembly showing the path a single ray might take while being viewed by the scanner. Although the basic theory of integrating spheres applies to the normal configuration mentioned earlier and not to this modified design, the basic principle is the same. Light collected by the fish-eye lens is scattered off the top side of the baffle and off the side walls until ultimately (assuming no absorption or loss through ports) it is reflected off the bottom half of the baffle where it is viewed by the scanner. Since the viewed radiation has been multiple-scattered and diffused, all angle effects should be minimized. This was a prime reason for considering an integrating sphere.

The major disadvantage of such a system, however, is the relatively low throughput. It can be shown that for an integrating sphere of surface area (S) and a detector port (b) located on the great circle normal to the entrance port great circle, the power received by the detector at (b) is:

$$Pr\ P\ \frac{b}{S}\left[\frac{1}{1 - r\frac{(S - b - a)}{S}}\right] \tag{10}$$

where P = power into sphere
b = area of exit (detector) port
a = area of entrance port
S = surface area of sphere
r = reflectivity of sphere side walls
Pr = power received by detector at b.

To roughly apply this relationship to the modified integrating sphere, one must account for the detector being removed from the surface of the sphere (i.e., not all the energy falling on the exit port is received by the scanner as it would be in the ideal case). Also, one must realize that the actual responsive region is not the exit port but is, instead, the baffle in the center of the sphere. Recognizing these limitations and applying Eq. (10) to actual parameters from one of the designs, i.e.,

r = 0.95
b = 1.50 in.
a = 1.0 in.
S = 51.31 sq. in. (7 in. diameter)

we get

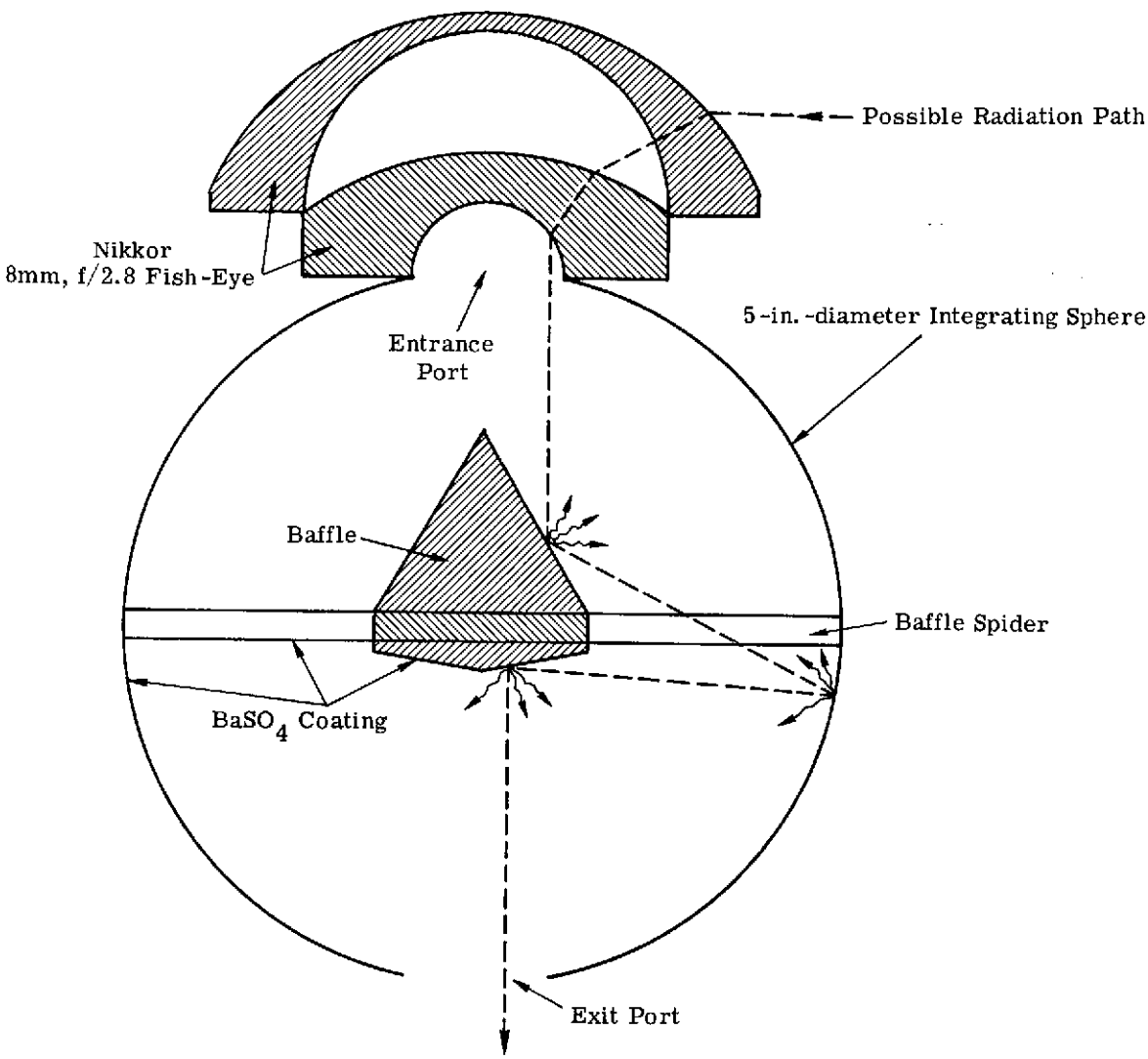

FIGURE 12. DIAGRAM OF FISH-EYE/INTEGRATING SPHERE LENS ASSEMBLY

$$\frac{Pr}{P} = \frac{b}{S}\frac{1}{\left[1 - r\frac{(S - a - b)}{S}\right]}$$

$$= 0.0040$$

or 0.40% throughput. The measured value for this same sphere was 0.59%, so one can see that the modified integrating sphere compares with theory somewhat reasonably.

3.2.3 INTEGRATING SPHERE TESTING

The same equipment layout and procedures used to test the mirror system were also employed in the testing of the refractive sky-reference design. Basically, the lens of the simulated scanner was imaged by an 11-in.-diameter lens with a 16.7 in. focal length onto the 1-1/2 in. diffuser baffle in the center of the sphere. Figures 13 and 14 show the test apparatus (minus black baffles) set up for measurements. In general, two measurements were made for each design. One evaluated the throughput versus source angle by maintaining the simulated scanner axis perpendicular to the sphere-lens apparatus and rotating the 200W lamp about the image of the fish-eye lens. A second measurement evaluated the receiver angle variation by maintaining the lamp at one fixed position and rotating the simulated scanner about the scanner lens.

Several differently shaped baffles were experimented with (see Fig. 12), as were a number of surface coatings and different sized spheres. Figure 15 shows the Fresnel lens and integrating sphere mounted together. For the double fish-eye lens arrangement, the entrance port on the sphere was 1.0 in. in diameter while for the single, larger lens, the entrance port was 2.50 in. in diameter. In all cases, the exit port was 1.0 in. in diameter. Two sphere sizes were chosen for testing based on trade-offs between throughput, angular response, and practical implementation; one was 7 in. in diameter and the other 5 in. Two sphere coatings were tried, $BaSO_4$ and flame-sprayed aluminum, as well as three baffle surfaces of polished aluminum, $BaSO_4$, and 3M white paint.

The results of all these tests are shown in Table 3. In general, the coatings on the baffles or their shapes made only minor impact on overall performance. The 5 in. sphere did, however, approximately double the throughput as compared to the 7 in. sphere (as one might anticipate from Eq. (10). For most cases, the response was flat to ±1% over approximately 1.5^{o} to 2.0^{o} of simulated scanner rotation. The response versus source angle, however, showed wide variations in lens and sphere size. The worst case consistently appeared when just the single-element fish-eye lens was used. This lens did have the best throughput, however.

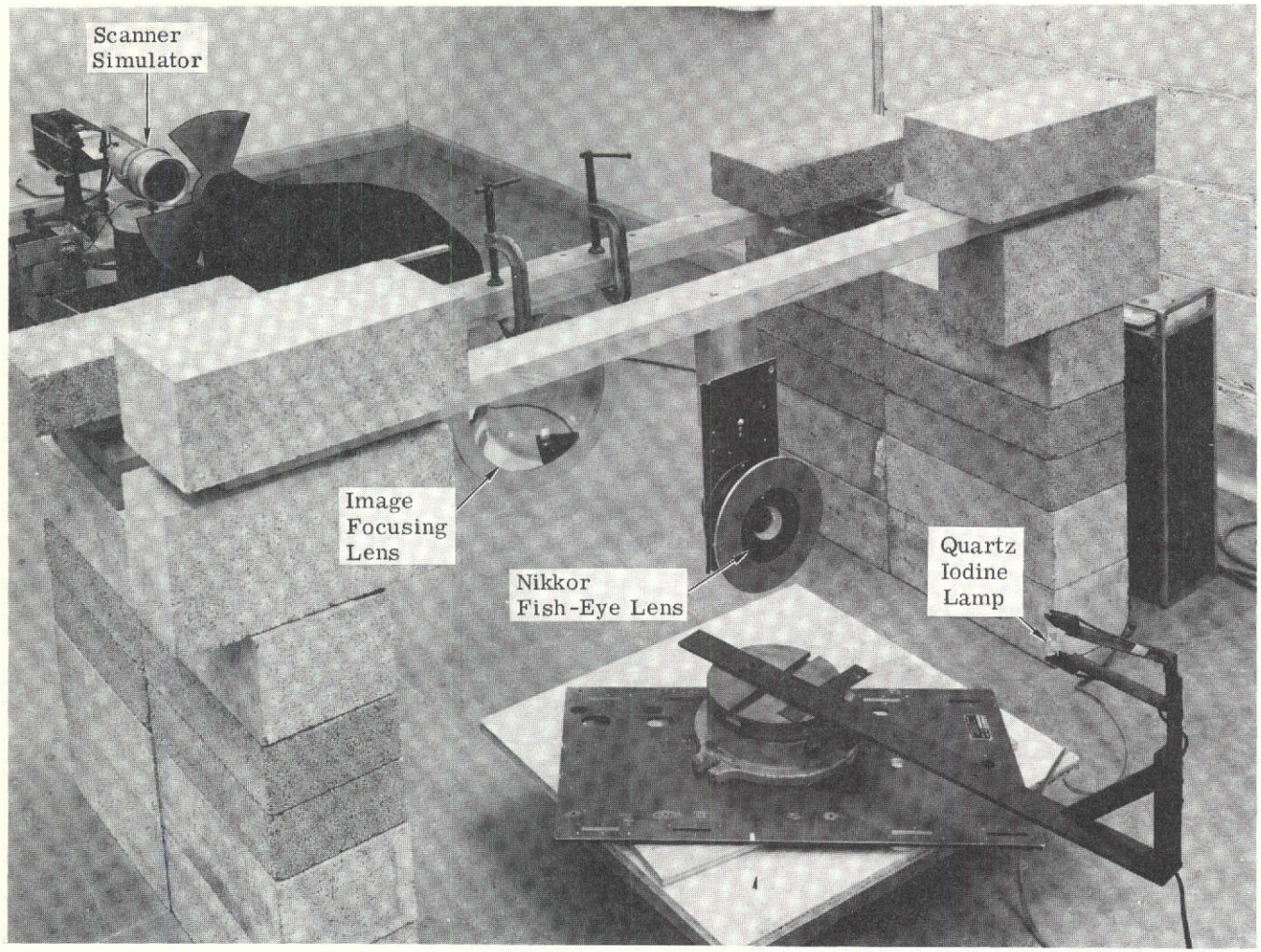

FIGURE 13. FISH-EYE/INTEGRATING SPHERE SETUP, VIEW 1

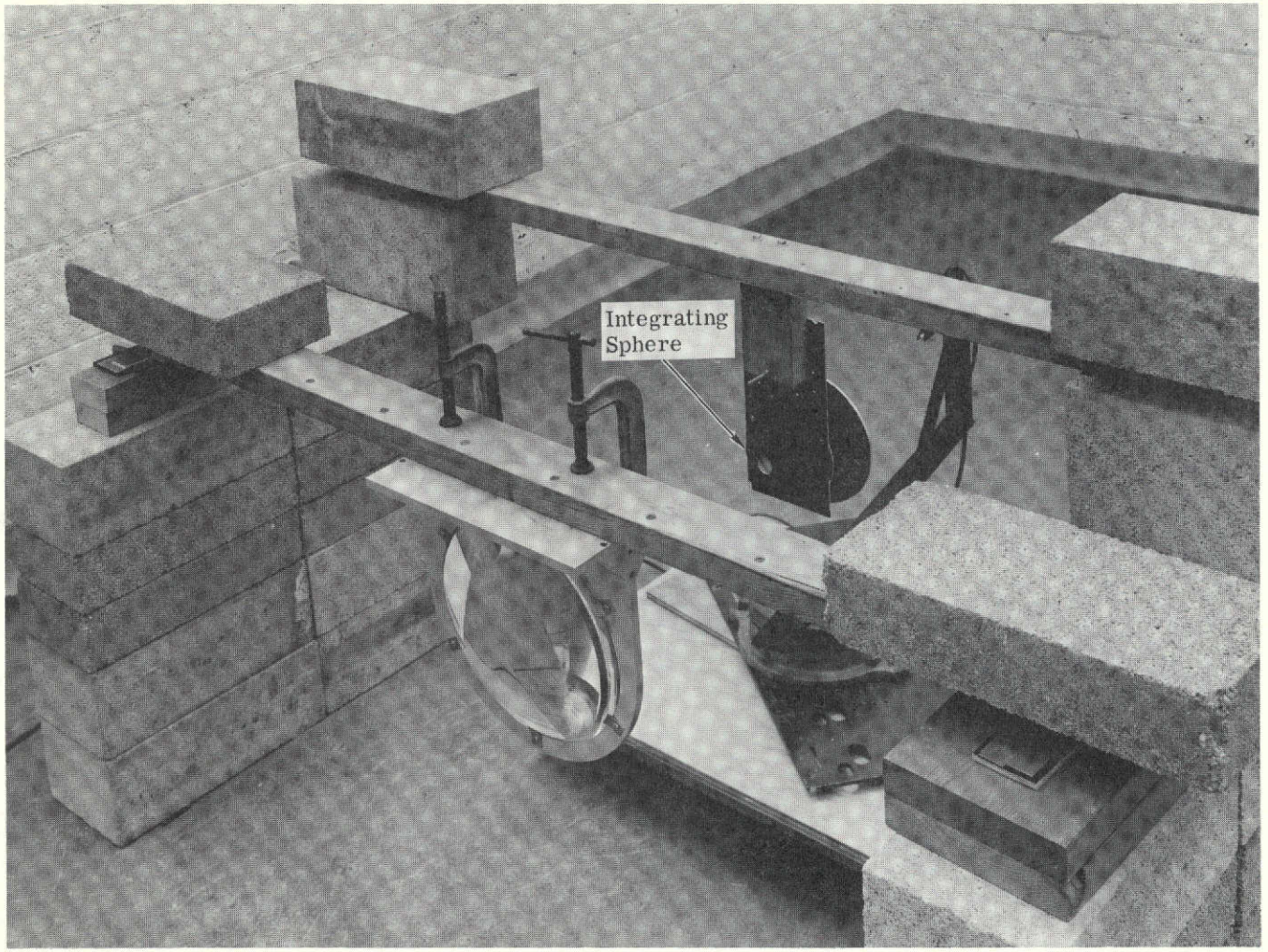

FIGURE 14. FISH-EYE/INTEGRATING SPHERE SETUP, VIEW 2

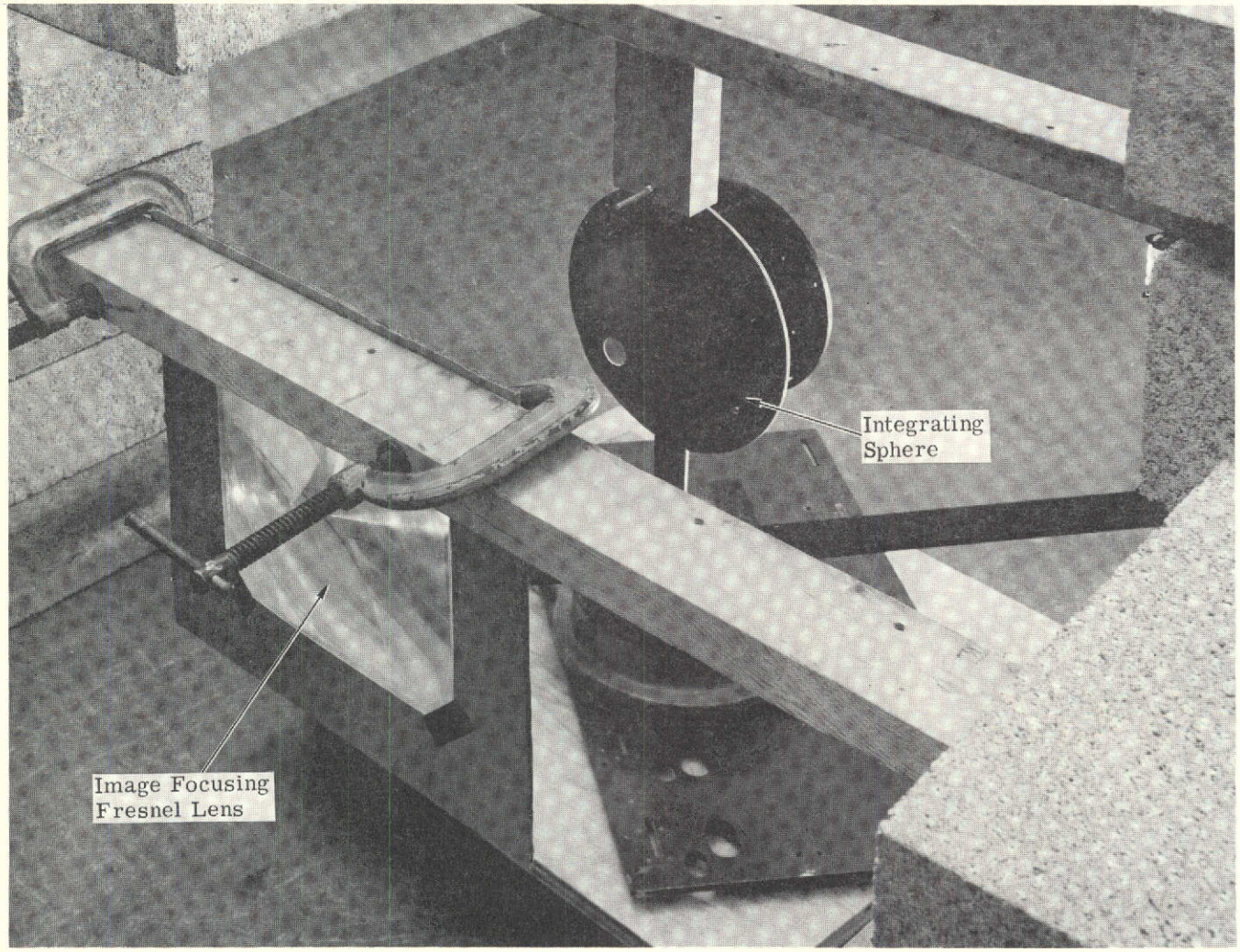

FIGURE 15. FISH-EYE/INTEGRATING SPHERE/FRESNEL LENS SETUP

TABLE 3. FISH-EYE LENS/INTEGRATING SPHERE TEST RESULTS

Sphere Diameter ($BaSO_4$ Coated) (in.)	Fish-Eye Lens Configuration	Entrance Baffle*	Exit Baffle** (cone)	50% Spectral Bandwidth (μm)	Throughput at 0^0 Zenith Angle and 0^0 Scan Angle (%)	Decrease (in Throughput) at 50^0 Zenith Angle and 0^0 Scan Angle (%)	Decrease (in Throughput) at 70^0 Zenith Angle and 0^0 Scan Angle (%)	Worst-Case Variation (%) Over Scan Angle (^{0})
7	double	$BaSO_4$ cone	$BaSO_4$	0.4-1.0	0.6	2.5	18.5	±1.0 over 2.0
7	double	polished Al cone	$BaSO_4$	0.4-1.0	0.6	10.0	24.0	±1.0 over 2.0
7	double	$BaSO_4$ cone	polished Al	0.4-1.0	0.4	8.0	19.0	—
5	double	$BaSO_4$ cone	$BaSO_4$	0.4-1.0	1.1	10.0	25.0	±1.0 over 1.2
7	single	$BaSO_4$ cone	$BaSO_4$	0.4-1.0	7.5	25.0	52.0	±2.5 over 2.2 and ± 1.0 over 1.7
7	single	2.83 in. black disk	$BaSO_4$	0.4-1.0	3.1	0	27.0	±1.0 over 2.4
5	single	2.90 in. black disk	$BaSO_4$	0.4-1.0	2.6	2.0	0	—
5	single	2.83 in. black disk	$BaSO_4$	0.4-1.0	3.0	5.0	5.0	±1.0 over 1.6
5	single	2.60 in. black disk	$BaSO_4$	0.4-1.0	3.6	15.0	20.0	—
5	single	2.00 in. black disk	$BaSO_4$	0.4-1.0	6.5	23.0	37.0	—
5	single	1.00 in. black disk	$BaSO_4$	0.4-1.0	8.7	27.0	49.0	—
7***	single	$BaSO_4$ cone	$BaSO_4$	0.4-1.0	2.1	24.0	70.0	—

*For 7 in. spheres, cone is 1.5 in. in diameter and 2.0 in. high; for 5 in. spheres, cone is 1.5 in. in diameter and 1.5 in. high.

**Cone is 1.5 in. in diameter and 0.25 in. high.

***Top-half is flame-sprayed Al, not $BaSO_4$ coated.

To obtain a more uniform response with the single lens, black disks of various diameters were tested in place of the upward-looking baffle in the sphere. This resulted in making the response versus source angle flatter but at the expense of throughput. Still, in terms of overall performance this particular baffle design, with the single lens and 5 in. sphere coated with $BaSO_4$ (and the 1-1/2 in., $BaSO_4$, flat exit-diffuser), provided the best experimental data for the fish-eye/integrating sphere configuration. With a throughput of only 2.6% at 0^o zenith source angle, it was only marginally acceptable (see Table 1). Figures 16 and 17 show the experimental data for response versus source angle and response versus receiver angle.

3.2.4 DIFFUSING GLASS DESIGN AND TESTING

Because of the low throughput encountered with the integrating sphere, diffusing glass was considered as an alternative. For the tests, the diffusing glass was placed behind the fish-eye lens for both the single- and the double-lens configurations. The circular area of illumination for the single lens was approximately 2-1/2 in. in diameter and for the double lens approximately 1-1/2 in. (larger than the lens exiting aperture because of the diffuser's thickness). Figure 18 shows a cross section of the fish-eye lens/opal glass arrangement. To expand this smaller area slightly and to insure that the scanner's field of view was being filled, tests were also made with the diffusing glass displaced 3/16 in. back from the lens. Figure 19 shows the mounting of the diffusing glass and fish-eye lens.

Two types of diffusing glass were tested, the results of which are shown in Table 4. The testing apparatus and procedure were identical to those used previously. The results showed that ground glass had the highest throughput but the worst diffusing characteristics.

The opal glass, even though it had a much lower throughput (approximately 4.6%), had a much better angular response curve. Figures 20 and 21 show its response versus source and receiver angles for the double lens configuration (the single lens did not fare well in this test). Throughput was down only 3% at 70^o zenith angle, and receiver angle variations were found to be ±1% over 1.4^o of scanner rotation.

These values were obtained with broadband measurements covering the region from 0.4 μm to 1.0 μm. Using an unfiltered silicon detector, tests were also conducted with narrowband interference filters to isolate any problems caused by a lessening of diffusing characteristics with increased wavelength. As can be seen from the data in Table 4, an angular variation does appear at the longer wavelengths, but this effect is caused mostly by a shifting of the illumination area on the opal glass and not by a decrease in throughput. Hence, either by making the image of the scanner mirror on the diffuser slightly larger than the maximum illumination area expected or by moving the image of the scanner mirror across the diffuser and thereby "searching" for the illuminated area, this potential angle response problem can

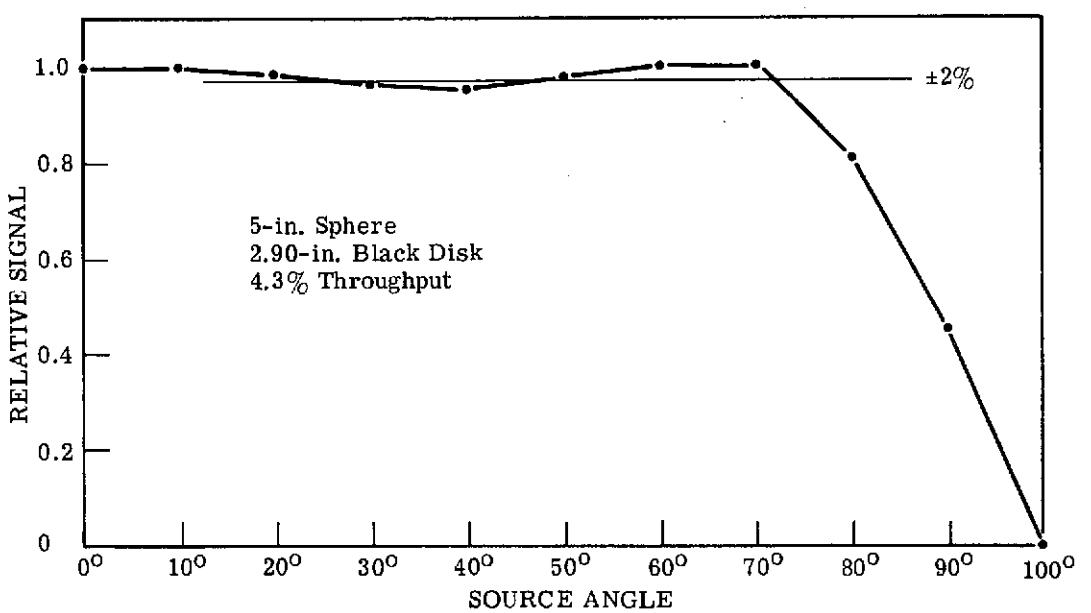

FIGURE 16. RELATIVE SIGNAL VERSUS SOURCE ANGLE FOR FISH-EYE/INTEGRATING SPHERE

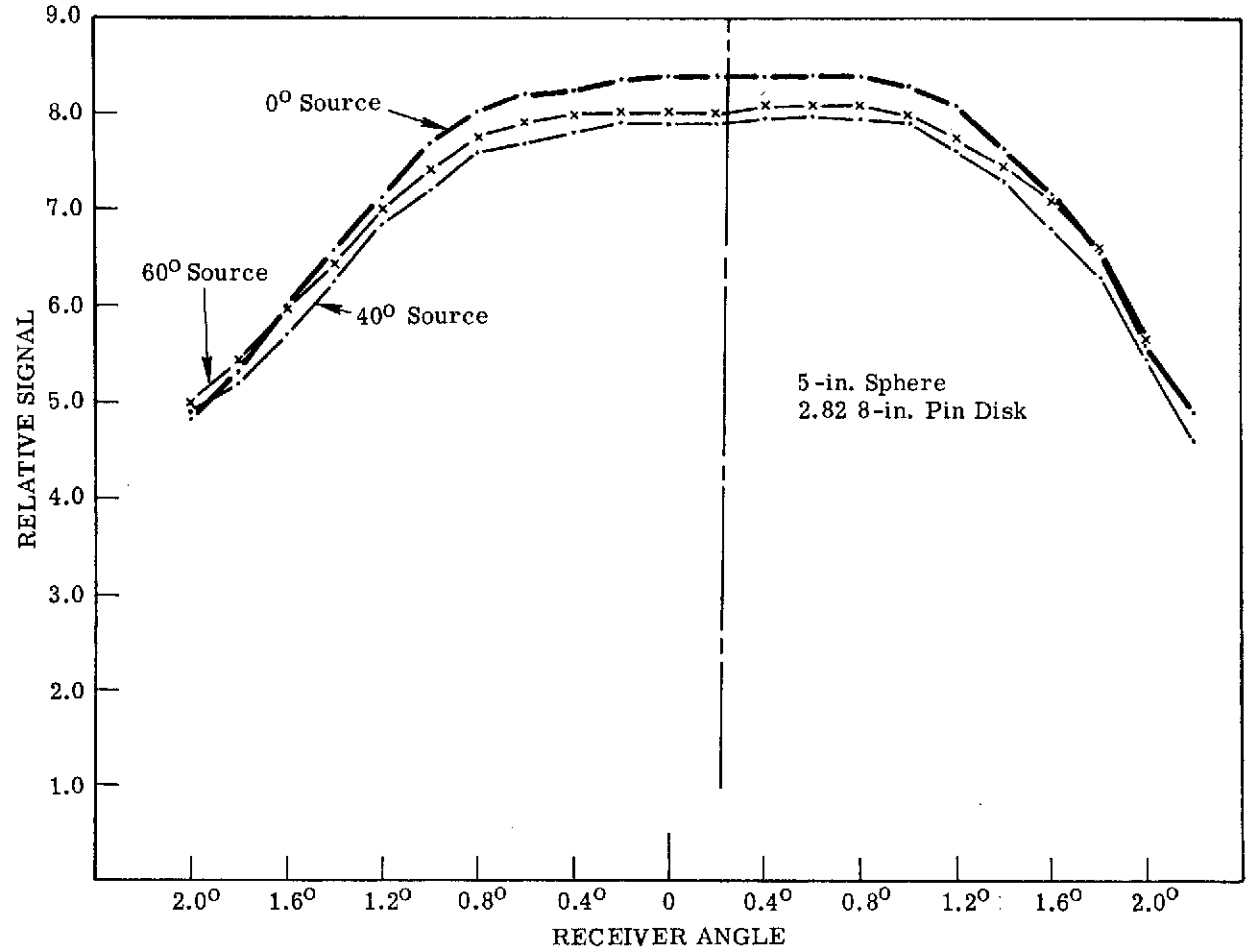

FIGURE 17. RELATIVE SIGNAL VERSUS RECEIVER ANGLE FOR FISH-EYE/INTEGRATING SPHERE. λ = 0.40-1.0 μm.

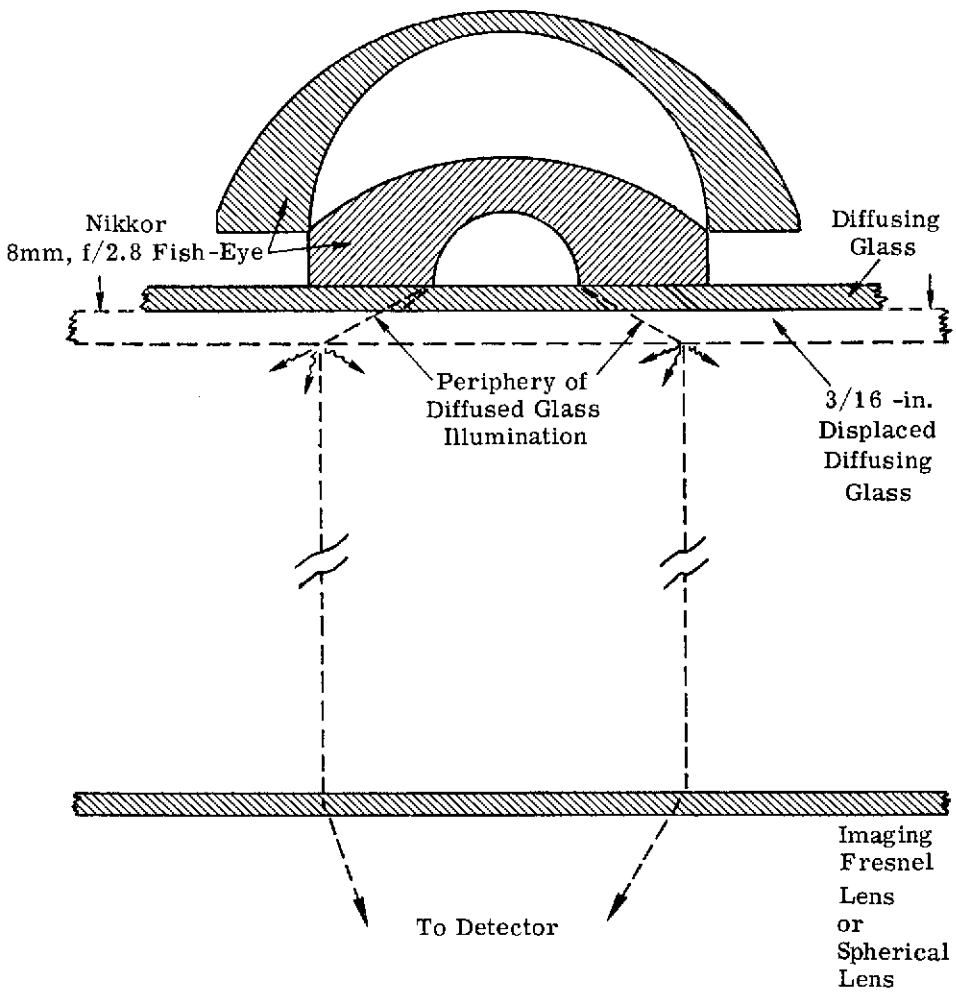

FIGURE 18. DIAGRAM OF FISH-EYE/OPAL GLASS/FRESNEL LENS ASSEMBLY

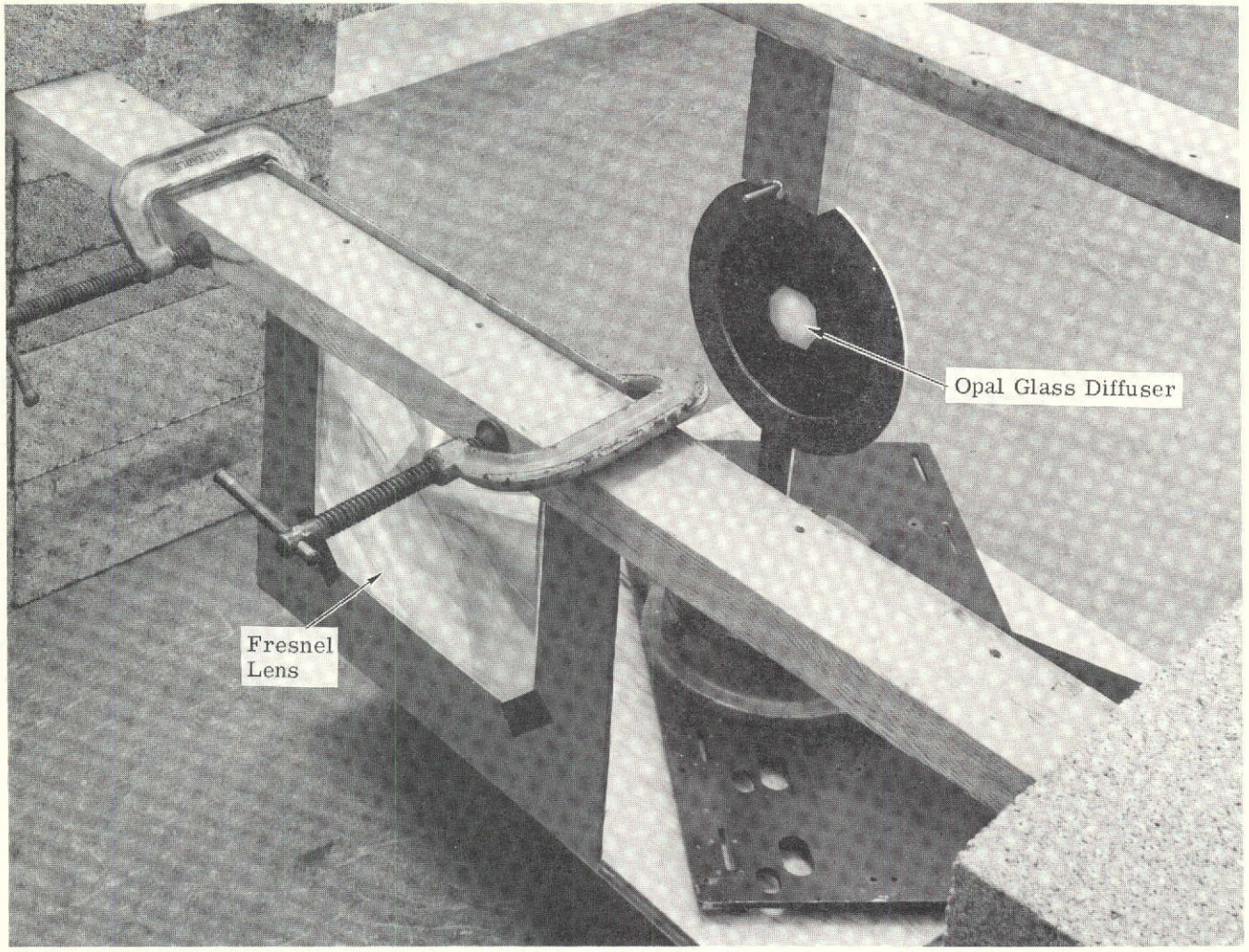

FIGURE 19. FISH-EYE/OPAL GLASS/FRESNEL LENS TEST SETUP

TABLE 4. FISH-EYE LENS/DIFFUSING GLASS TEST RESULTS

Fish-Eye Lens Configuration	50% Spectral Bandwidth (μm)	Glass Distance Behind Lens (in.)	Diffuser	Throughput at 0° Zenith Angle and 0° Scan Angle (%)	Decrease (in Throughput) at 50° Zenith Angle and 0° Scan Angle (%)	Decrease (in Throughput) at 70° Zenith Angle and 0° Scan Angle (%)	Worst-Case Variation (%) over Scan Angle (°)
double	0.4-1.0	0	ground glass	52.8	53.0	86.0	—
double	0.4-1.0	0	ground glass and Fresnel lens	68.0	81.0	92.0	—
double	0.4-1.0	0	opal	5.7	5.0	15.0	—
double	0.4-1.0	3/16	opal	4.6	1.0	3.0	±1.0 over 14
single	0.4-1.0	5/16	opal	13.5	11.5	28.0	—
double	0.47-0.48	3/16	opal	—	1.0	1.0	±1.5 over 1.6
double	0.56-0.57	3/16	opal	—	1.0	2.0	—
double	0.63-0.64	3/16	opal	—	1.5	6.0	—
double	0.70-0.71	3/16	opal	—	3.5	8.5	—
double	0.80-0.81	3/16	opal	—	4.5	9.5	—
double	1.00-1.01	3/16	opal	—	8.5	17.0	±1.5 over 1.6
double	1.00-1.01	3/16	opal	—	3.0*	6.0* **	—
double	1.00-1.01	3/16	1.0 in. opal	—	2.5	9.5	—
double	1.00-1.01	3/16	1.5 in. opal	—	0	2.5	—
double	1.00-1.01	3/16	2.0 in. opal	—	0	4.0	—
double	1.00-1.01	0	1.5 in. opal	—	1.5	3.5	—
double	1.00-1.01	0	2.0 in. opal	—	0	4.0	—
double	1.00-1.01	3/16	opal and Fresnel lens	—	1.5	7.5	±1.0 over 2.8

*% decrease from maximum signal.

**Scan angle for maximum signal shifts 1.5° for a 70° source zenith angle at 1.0 μ.

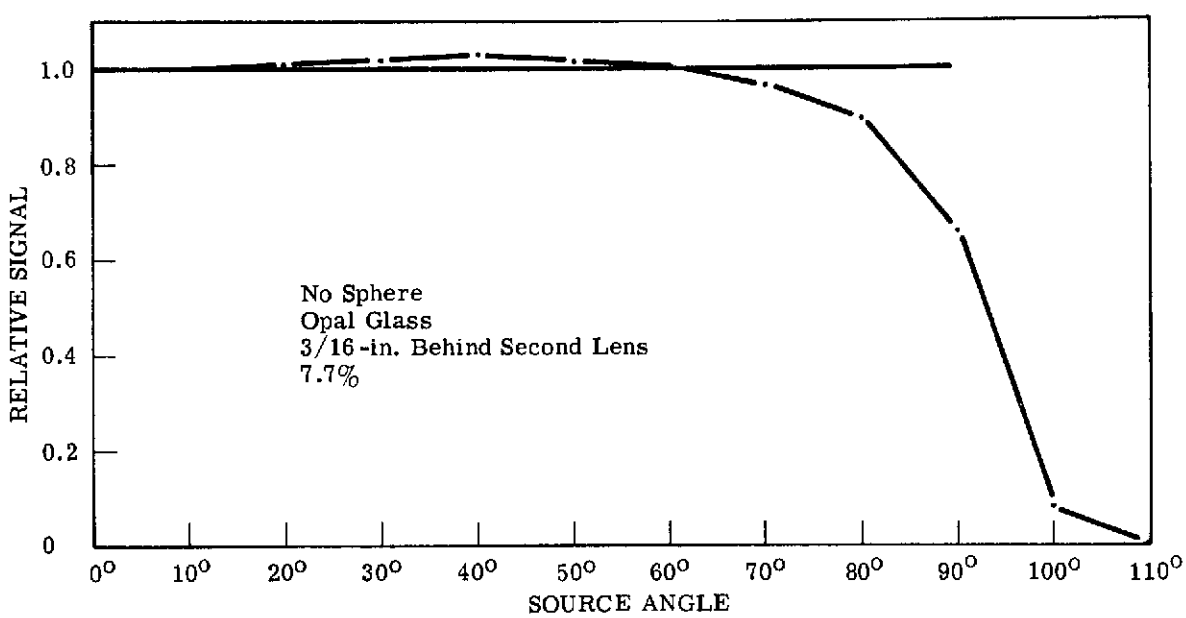

FIGURE 20. RELATIVE SIGNAL VERSUS SOURCE ANGLE FOR FISH-EYE/OPAL GLASS/ FRESNEL LENS

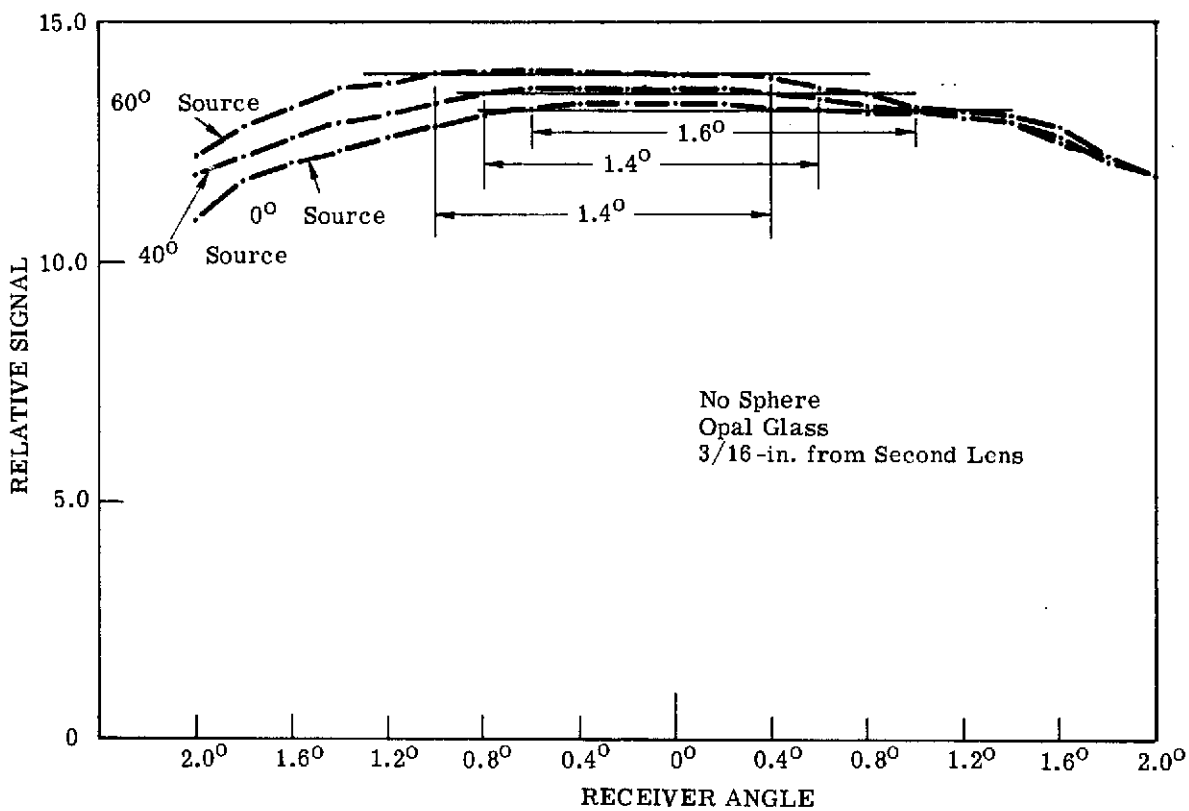

FIGURE 21. RELATIVE SIGNAL VERSUS RECEIVER ANGLE FOR FISH-EYE/OPAL GLASS/ FRESNEL LENS. λ = 0.40-1.0 μm.

be reduced to a negligible value up to 1.0 μm. Maximum decrease in signal (at 1.0 μm) by doing this would be approximately 6% at 70° zenith angle. Additional help would come from a Fresnel lens in place of the 11-in.-diameter spherical lens used to image the scanner mirror on the opal glass.

4
DESIGN OF AN APPARATUS TO BLOCK THE SUN

One of the motivations in designing a new sky reference was the possibility of measuring more than just total solar irradiance with the new device. For instance, the amount of atmospheric haze present at the time of a remote earth observation is very important since any haze will scatter and absorb parts of the radiation measured. The effects of haze on remote sensing have been modeled [2], but data are still needed to define adequately the atmospheric state if the model is to be used correctly.

Unfortunately, not enough is known about the model and the atmosphere as a whole to fully define what parameters need to be measured. Obviously, the total solar irradiance alone is not enough since most, but not all, of the signal comes from the sun itself. More information is required about scattered radiation; this necessitates blocking the sun for a portion of the measurement. This basic requirement could be satisfied by a rotating vane placed on the optical axis of the sky reference, but several questions remain unanswered. The most important question is: How much of the sun/sky can we block and still provide useful information about haze content? Obviously, the wider the rotating vane, the more data points have to be averaged to reduce noise; and with the sun blocked, noise is a serious problem.

Other concerns also affect the design of such an apparatus. The size must be limited to permit installation in an aircraft. The rate of the rotating vane must be optimized so that the number of sun-blocked signals is high enough to permit proper analysis, while at the same time low enough that they repeat themselves within a reasonable number of scan lines. Also, accuracy of the device must be maintained within reasonable limits. This means keeping the amount of stray radiation to a minimum and carefully studying the system noise and S/N ratio.

The particular design considered was a hemispherical vane which would block out a pie-wedged section of the sky while rotating about the optical axis of the sky reference. Since the vane would block out the sun at some point during its rotation almost regardless of the sun's elevation, it thereby would provide a haze measurement. There are, obviously, some trade-offs encountered in such a design. The question of vane size presents a key hurdle in the implementation of this device. Other trade-offs were discussed earlier. Although considerable effort was placed on the fabrication aspect of the problem, little, if any, has been expended on the modeling. Further studies should be made not only on the model itself but also on the operational aspect. Means to use this new information in an operational mode should be demonstrated before significant effort is put in fabrication. We cannot make recommendations about an apparatus to block the sun until further information is obtained.

5
PREAMPLIFIER STUDY FOR ARRAY 1 OF MSDS

5.1 INTRODUCTION AND SUMMARY

This study was undertaken to find ways of improving noise equivalent reflectance by reducing the noise level of silicon detector channels on the MSDS. We made theoretical and experimental evaluation of the originally delivered preamplifiers and the first stage of an improved hybrid preamplifier. A fivefold improvement with the hybrid has been measured with a detector operating at the full bandwidths required for the MSDS at maximum V/H = 0.18. A larger improvement factor is expected when operating at a reduced bandwidth with lower V/H.

We propose that the Array 1 circuitry of the MSDS be modified to include a hybrid stage between the present detectors and the original preamplifier. It is expected that this would result in a substantial improvement in MSDS performance for these channels. This modification can best be done at JSC, and the authors would be glad to provide advice on design details.

5.2 THEORY OF DETECTOR-PREAMPLIFIER RESPONSE*

In this section, the output response of the detector-preamplifier circuit will be determined in terms of circuit parameters. The equivalent circuit shown in Fig. 22 will be used. The symbols from this figure are defined below:

i_s = detector equivalent current source caused by signal (amp)

i_d = detector equivalent current source caused by noise (amp-Hz$^{-1/2}$)

i_a = equivalent current source caused by noise in the operational amplifier (OA), with the input open-circuited (amp-Hz$^{-1/2}$)

e_a = equivalent voltage source caused by noise in the OA, with the input short-circuited (V-Hz$^{-1/2}$)

e_f = equivalent voltage source caused by Johnson noise in the feedback impedance

e_o = amplifier-output response (V-Hz$^{-1/2}$)

Z_f = feedback impedance (assumed to be a resistor, R_f, in parallel with a capacitor, C_f)

R_d = equivalent detector-shunt resistance (Ω), which includes the detector resistance in parallel with the OA-input resistance (Ω)

*Part of this Section appeared in the report cited in Ref. [3].

C_d = equivalent detector-shunt capacitance, including junction capacitance, connecting lead capacitances to ground, stray capacitance of OA summing point to ground, and input capacitance of the OA(f)

Z_d = detector impedance, which includes R_d in shunt with $C_d(\Omega)$

μ = gain and dynamics of the actual OA, with infinite input impedance and without noise (unitless)

Each source (currents and voltages) will be considered separately, when the amplifier-output response is derived. Superposition will then be assumed, and the output responses will be added in a root-sum-squared form, so that

$$i_3 = \sqrt{i_1^2 + i_2^2} \equiv i_1 \dotplus i_2$$

Figure 1 is redrawn as Fig. 2, but only sources i_s, i_d and, i_a are considered, where

$$i_z \equiv i_d \dotplus i_s - i_a$$

In Fig. 23, the voltage input, ϵ, to the ideal OA is $-e_o/\mu$. The current i_z is split between Z_d and Z_f, leading to the following equation:

$$i_z = \frac{\epsilon}{Z_d} + \frac{\epsilon - e_o}{Z_f} = \frac{-\left(\frac{e_o}{\mu}\right)}{Z_d} + \frac{-\left(\frac{e_o}{\mu}\right) - e_o}{Z_f}$$

which can be rewritten as

$$-e_o = \frac{i_d \dotplus i_a \dotplus i_a}{\frac{1}{Z_f} + \frac{1}{\mu}\left(\frac{1}{Z_f} + \frac{1}{Z_d}\right)} \tag{11}$$

Figure 22 is then redrawn as Fig. 24, but the only source considered is e_f. The input voltage to the OA, ϵ, is attenuated from e_f and e_o by the voltage dividing action of Z_d and Z_f and can be written as

$$\epsilon = -\frac{e_o}{\mu} = \frac{(e_f + e_o)Z_d}{Z_d + Z_f}$$

which can be solved for e_o to give

$$-e_o = \frac{\frac{e_f}{Z_f}}{\frac{1}{Z_f} + \frac{1}{\mu}\left(\frac{1}{Z_f} + \frac{1}{Z_d}\right)} \tag{12}$$

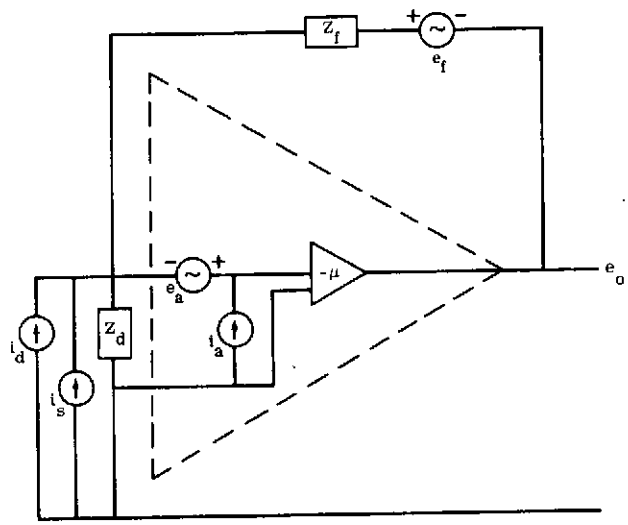

FIGURE 22. DETECTOR-PREAMPLIFIER EQUIVALENT CIRCUIT

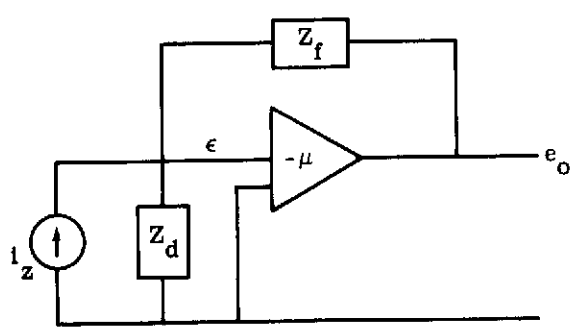

FIGURE 23. EQUIVALENT CIRCUIT IN WHICH ONLY THE CURRENT SOURCES IN FIG. 22 ARE CONSIDERED

Finally, Fig. 22 is redrawn as Fig. 25, and the only source considered is e_a. From the circuit, Fig. 25b, the response equation is

$$-\frac{e_o}{\mu} = \frac{e_o Z_d}{Z_d + Z_f} + e_a$$

which can be rewritten as

$$-e_o = \frac{e_a\left(\frac{1}{Z_f} + \frac{1}{Z_d}\right)}{\frac{1}{Z_f} + \frac{1}{\mu}\left(\frac{1}{Z_f} + \frac{1}{Z_d}\right)} \tag{13}$$

Because the noise source is assumed to be from the channel of the field-effect transistor (FET), e_a is assumed to be in the circuit after the input impedance.

Now, consider Z_f and e_f (referred to in Fig. 22) in more detail. In Fig. 26a and b the equivalent circuit of the actual components (part a) is defined in terms of the actual parameters (part b). $\sqrt{4KTBR_f}$ is the Johnson noise voltage of the resistor, R_f. Z_f is the parallel impedance of R_f and $1/C_fS$, where S is the Laplace operator (sec^{-1})

$$Z_f = \frac{R_f\left(\frac{1}{C_fS}\right)}{R_f + \left(\frac{1}{C_fS}\right)} = \frac{R_f}{R_fC_fS + 1}$$

The voltage divided from $\sqrt{4KTBR_f}$ by R_f and $1/C_fS$ is e_f, which can be written as

$$e_f = \frac{\frac{1}{C_fS}\sqrt{4KTR_f}}{R_f + \frac{1}{C_fS}}$$

The $\sqrt{\text{bandwidth}}$, $\sqrt{B}$, is dropped because e_f, e_a and e_o units are $V/\sqrt{Hz}$. Similarly, i_d, i_a and i_s units are amp-$Hz^{-1/2}$.

$$e_f = \frac{R_f}{R_fC_fS + 1}\sqrt{\frac{4KT}{R_f}} = Z_f\sqrt{\frac{4KT}{R_f}} \tag{14}$$

If we use superposition and Eqs. (11), (12), (13), and (14), the total response can be represented as

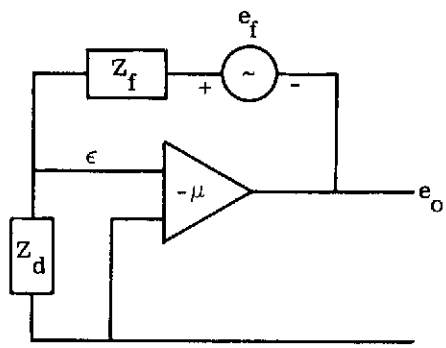

FIGURE 24. EQUIVALENT CIRCUIT OF FIG. 22 IN WHICH ONLY THE VOLTAGE SOURCE CAUSED BY JOHNSON NOISE IS CONSIDERED

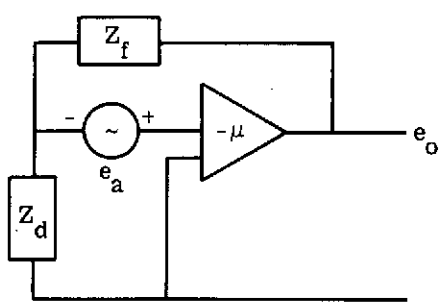

(a) Equivalent Circuit

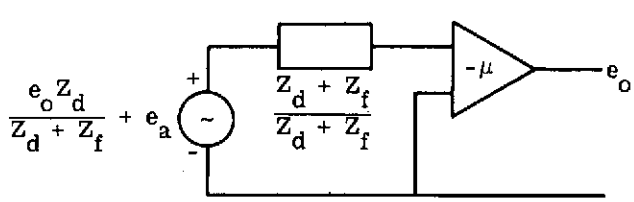

(b) Simplified Equivalent Circuit

FIGURE 25. EQUIVALENT CIRCUIT IN WHICH ONLY THE VOLTAGE SOURCE e_a IS CONSIDERED

$$-e_o = \frac{i_s + i_d + i_a + \sqrt{\frac{4KT}{R_f}} + e_a\left(\frac{1}{Z_f} + \frac{1}{Z_d}\right)}{\frac{1}{Z_f} + \frac{1}{\mu}\left(\frac{1}{Z_f} + \frac{1}{Z_d}\right)}$$

In addition, μ will be very large, and $1/\mu$ will approach zero. The denominator will approach $1/Z_f$.

The equivalent noise-current response is expressed as:

$$-\frac{e_o}{Z_f} \cong i_d + i_a + \sqrt{\frac{4KT}{R_f}} + e_a\left[\frac{1}{R_f} + \frac{1}{R_d} + (C_f + C_d)S\right] \equiv i_t \qquad (15)$$

where i_t is input-noise current. The signal response is

$$-\frac{e_o}{Z_f} \cong i_s$$

Commercial operational amplifiers do not perform as well as good available components; therefore amplifiers should be constructed from components. Low-noise FETS tend to have an e_a of 4 $nV/Hz^{1/2}$ and a negligible amount of i_a.

Low-noise, silicon, bipolar transistors (BPT) tend to have an e_a of 2 $nV/Hz^{1/2}$ and an i_a of 1 pico-amp/$Hz^{1/2}$. For any particular FET or BPT, the e_a and i_a will not have these exact values and will change as a function of frequency and bias, but the previous values serve to illustrate the expected relative magnitude of the input-noise currents.

The equivalent input-noise current is given by Eq. (15). From this equation and the previous e_a and i_a values, a summary of noise components (Fig. 27) is derived.

Z_x, defined as Z_d in parallel with Z_f, is the impedance from the OA summing point (input) to all other points. In Fig. 27, the dominant noise currents can be determined as a function of Z_x. For $Z_x < 4$ kΩ, a BPT is superior to an FET, and the dominant noise source is the e_a of the BPT. For $Z_x > 4$ kΩ, an FET is superior to a BPT, and the dominant noise can be either the FET or Johnson noise, depending on both Z_x and the resistors used.

With the exception of the component from e_a, equivalent input noise-current components of Eq. (15) are simple in concept. In Eq. (15), the output and components of input are considered to be per root hertz of bandwidth, and normally the noise over the integrated total bandwidth is desirable. Usually a good measure of the noise over the total bandwidth can be obtained if we consider only the noise at the high-frequency limit, f_h, of the system involved.

The component from e_a at the high-frequency limit can be dominated by either the resistive or the capacitive term, but the capacitive term usually dominates. In this particular case, where i_e is a function of frequency, the expression can be approximated as

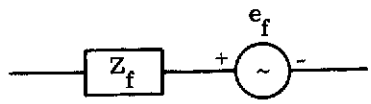

(a) Equivalent Circuit of the Actual Parameters

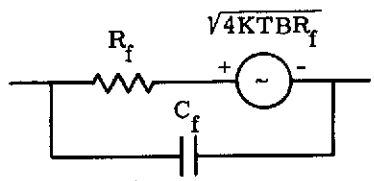

(b) Actual Parameters

FIGURE 26. FEEDBACK RESISTOR

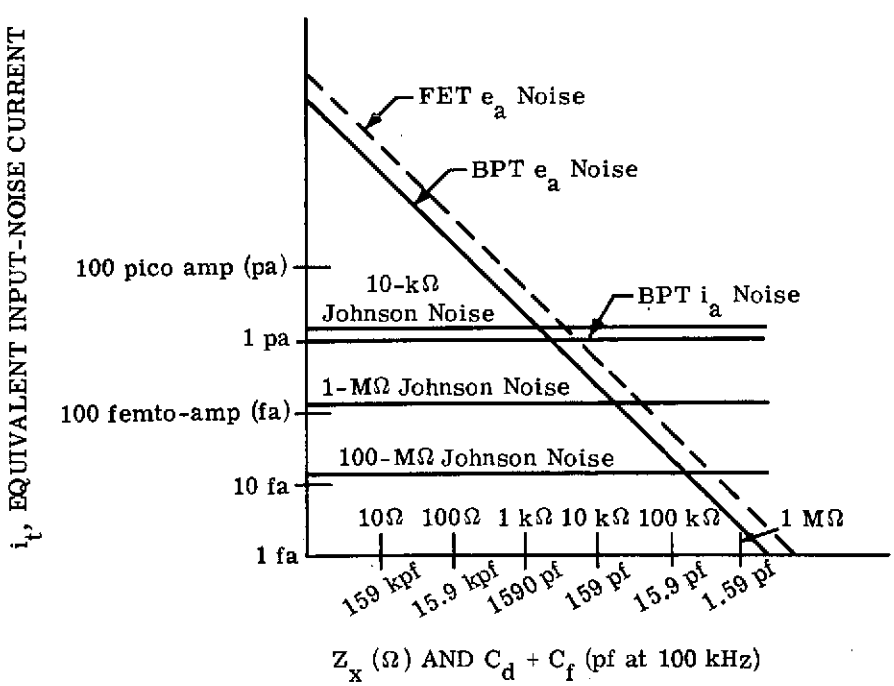

FIGURE 27. SUMMARY OF NOISE COMPONENTS

$$i_e \equiv e_a\left[\frac{1}{R_f} + \frac{1}{R_d} + (C_f + C_d)S\right] \cong e_a 2\pi f_h(C_f + C_d) \tag{16}$$

To reduce this component of noise, the e_a, the f_h, and the total capacitance from the OA summing point must be reduced to the practical limit.

5.3 THEORETICALLY DERIVED NOISE FOR ORIGINALLY DELIVERED PREAMPLIFIERS

The schematic of the original preamplifiers is shown in Fig. 28. The noise (referred to the input) expected from the dominant noise source is illustrated in Fig. 29 by the dashed lines. The current-noise from the 2N4019 input transistor was obtained from the manufacturer's data sheet. The equivalent current (i_e) was derived from the voltage-noise on the manufacturer's data sheet of approximately 3 $nV/Hz^{1/2}$ of bandwidth and from an assumed capacitance of 42 pf. This is based on a summation of the following estimated capacitances:

detector	25 pf
cable and connector	11 pf
2N4019 input	5 pf
across feedback and offset resistors	1 pf
total	42 pf

The Johnson or thermal noise contribution from the 1 megohm feedback resistor and the 1 megohm offset resistor is the root summed squared components from each resistor. The Johnson noise (i_j) from each is

$$i_j = \sqrt{\frac{4KT}{R}} = 1.28 \times 10^{-13} \text{ amp-Hz}^{-1/2}$$

where K = Boltzmans constant (1.38×10^{-23} W Hz^{-1} $^oK^{-1}$)

T = temperature of resistors (295 degrees Kelvin)

R = resistance (1 megohm).

The total Johnson noise from both resistors is $\sqrt{2}$ larger than this. The total theoretical noise at each frequency, plotted in Fig. 29 as a solid line, is the root summed squared components of each of the three dominant sources.

5.4 THEORETICALLY DERIVED NOISE FOR THE HYBRID FIRST STAGE

The schematic of the total circuit tested is shown in Fig. 30.

The noise (referred to the input) expected for this circuit from the dominant noise sources are plotted in Fig. 31. The current noise from an FET is usually negligible. The Johnson noise can be calculated similarly to the previous calculation except that using a 20 megohm resistor results in a Johnson noise of 2.85×10^{-14} amp-$Hz^{-1/2}$. The equivalent current-noise

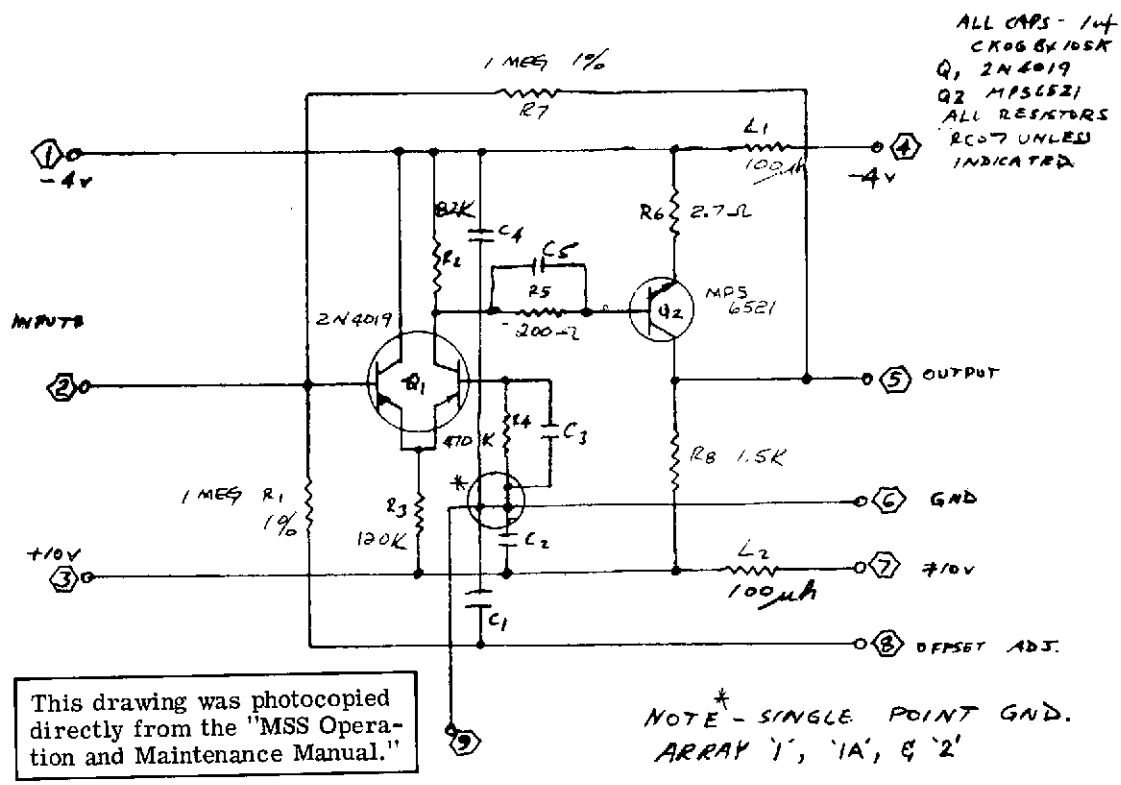

This drawing was photocopied directly from the "MSS Operation and Maintenance Manual."

FIGURE 28. PREAMPLIFIER (ARRAYS 1 AND 2), SCHEMATIC DIAGRAM

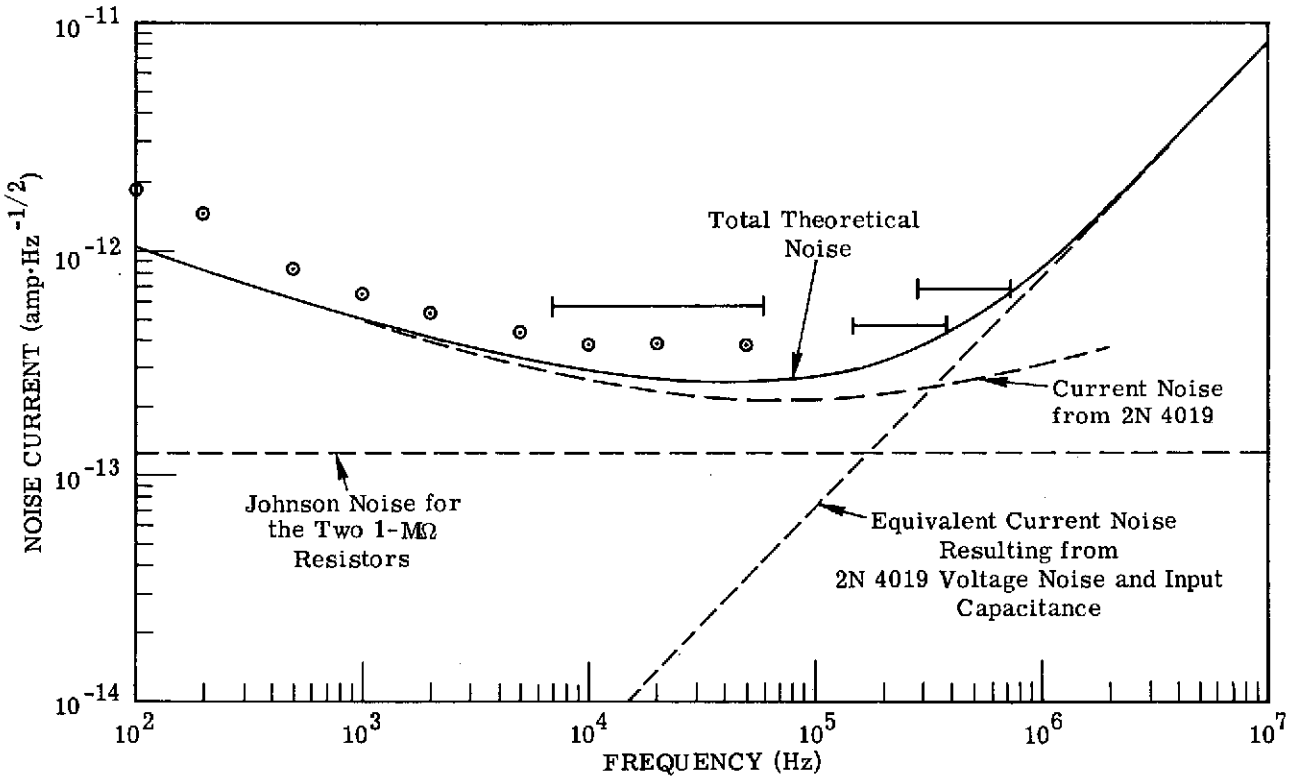

FIGURE 29. NOISE COMPONENTS FROM THE ORIGINALLY DELIVERED PREAMPLIFIERS

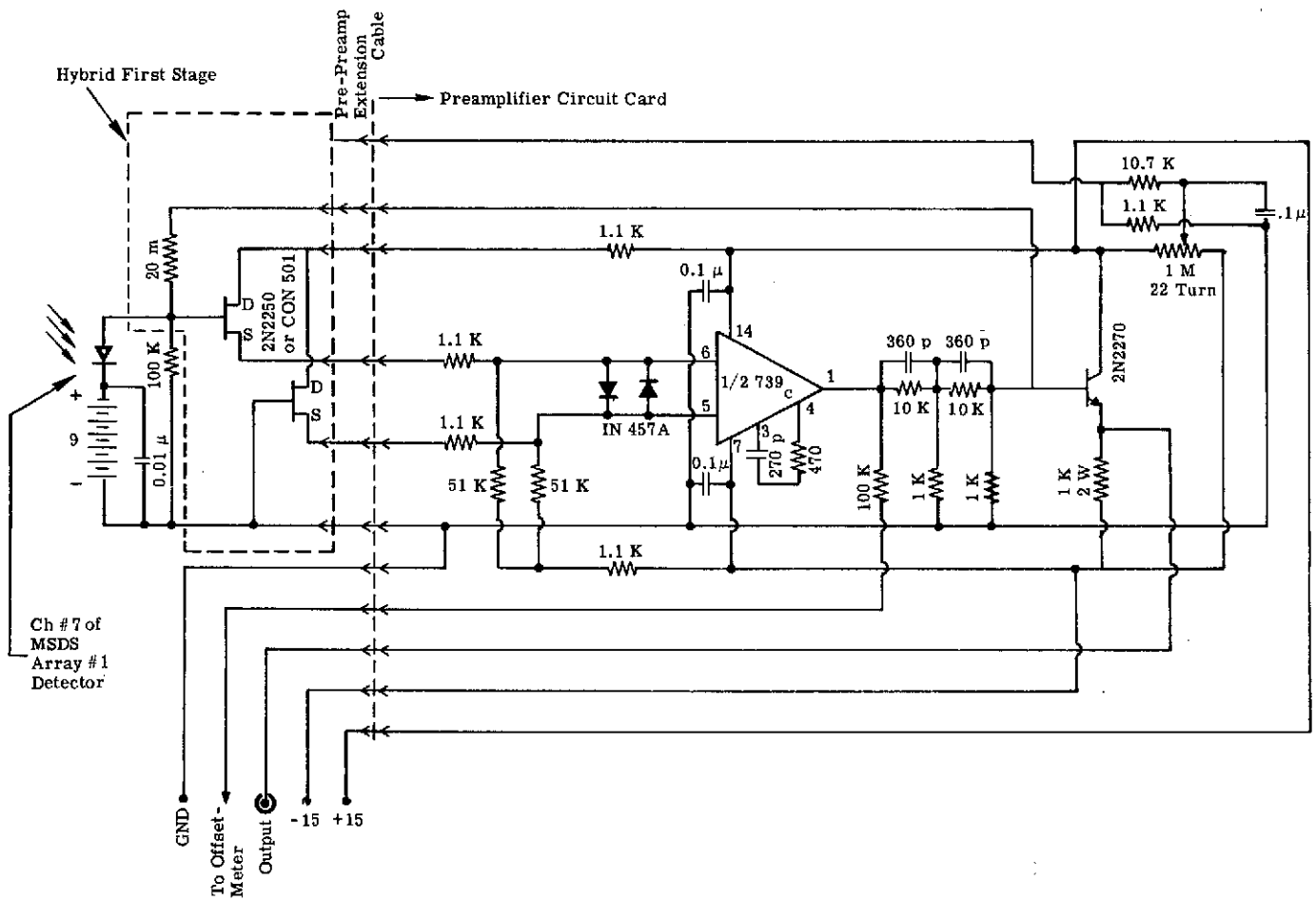

FIGURE 30. HYBRID FIRST-STAGE TEST CONFIGURATION

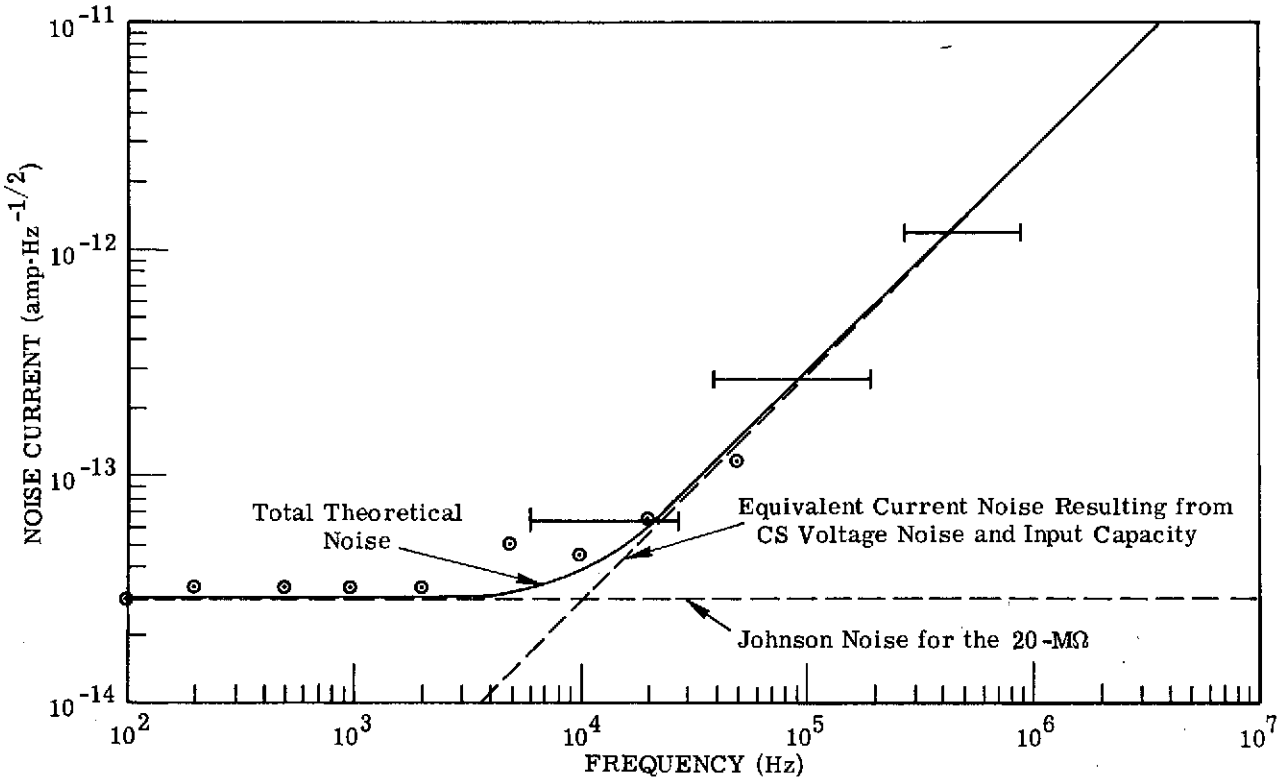

FIGURE 31. NOISE COMPONENTS FOR THE HYBRID CIRCUIT

was derived from a noise voltage using the manufacturer's data sheet and an estimated capacitance of 42 pf. This assumption was made to permit agreement with the test configuration. This allowed the same input capacitive circuit to be used when testing both the original and hybrid circuits. This assumption, however, will result in too high a value of noise when used with an actual detector since cable and connectors are not envisioned as being between the detector and the hybrid first stage. The total theoretical noise at each frequency is also plotted in Fig. 31.

5.5 PREAMPLIFIER NOISE MEASUREMENTS

Both the original and hybrid first stage were fabricated and noise measurements made on each. The measured values, plotted in Figs. 29 and 31 respectively, show close correlation with theoretical values. The circled dots are measurements made with an HP 302A Harmonic Analyzer and a nominal 7-Hz bandwidth. The horizontal bar measurements were made with a built-up bandpass filter. The extent of each bar represents the frequencies between the equivalent square bandwidth of the combined amplifier and filter response. These bars indicate that these measurements are relatively broadband ones. The preamplifier input was connected to a capacitive source of 36 pf to simulate a detector, cable, and connectors. The same source was used for both circuits. Photographs of the hybrid test circuit as tested are shown in Figs. 32 and 33. The FET chips are Siliconix (model CDN-S01), and the resistor chip is a 20 megohm resistor (model 112) from Eltec Instruments, Inc.

Considering the fact that these are noise measurements, the agreement between theoretical total noise and measured points is reasonable.

5.6 DETECTOR-PREAMPLIFIER NOISE MEASUREMENT

The Channel #7 detector-element from the first 1A array installed on the MSDS was coupled into each preamplifier and illuminated with a GaAs diode at a range of 1.4 in. A 100-Hz squarewave current was inserted into the light-emitting diode. Photographs presented in Fig. 34 show the response from each amplifier. With the hybrid circuit there is considerable improvement in signal to noise as compared to the original preamplifier. The low frequency waviness in the chip photograph was later traced to the power supply, but more photographs were not taken.

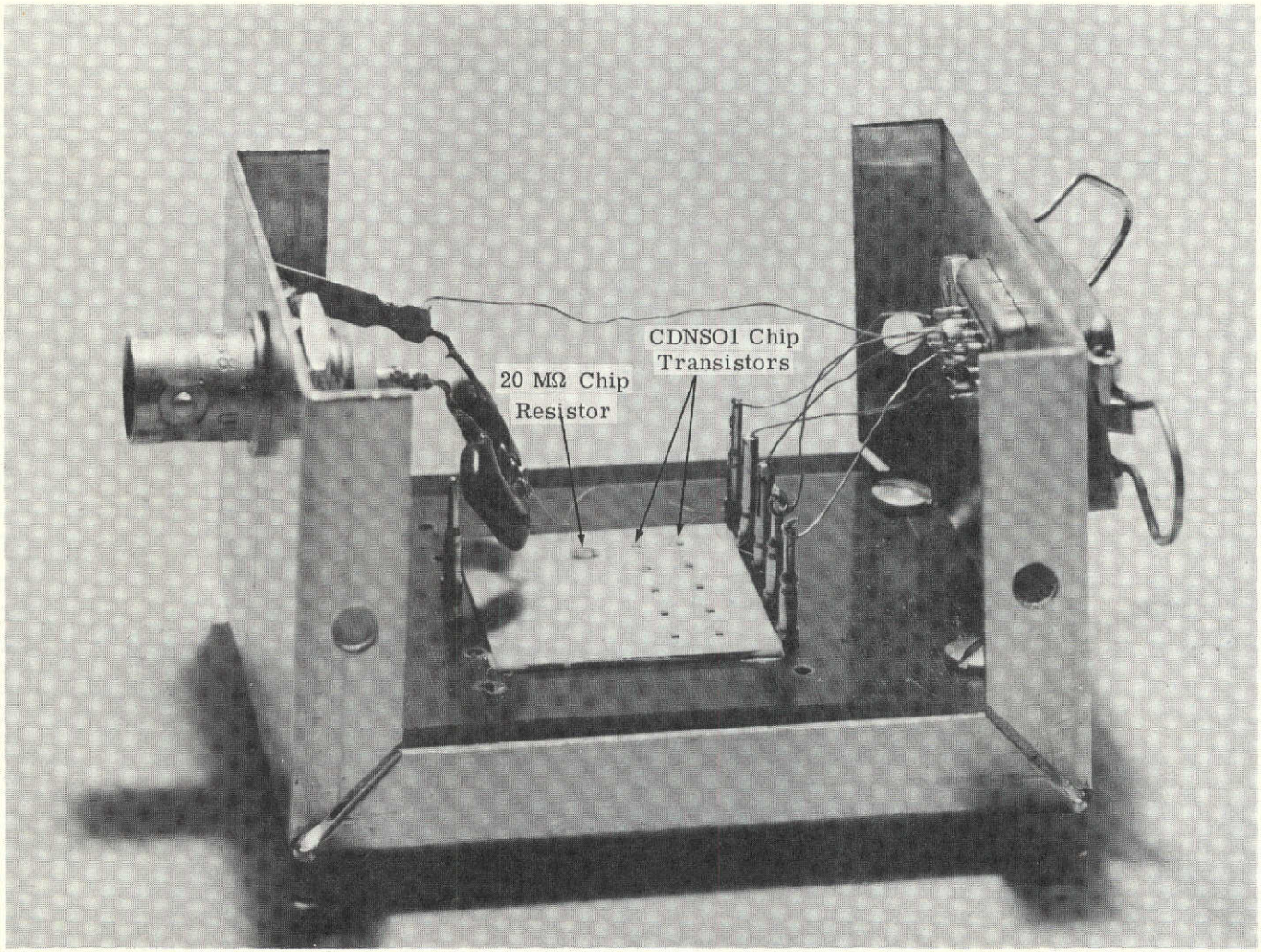

FIGURE 32. HYBRID FIRST-STAGE BREADBOARD

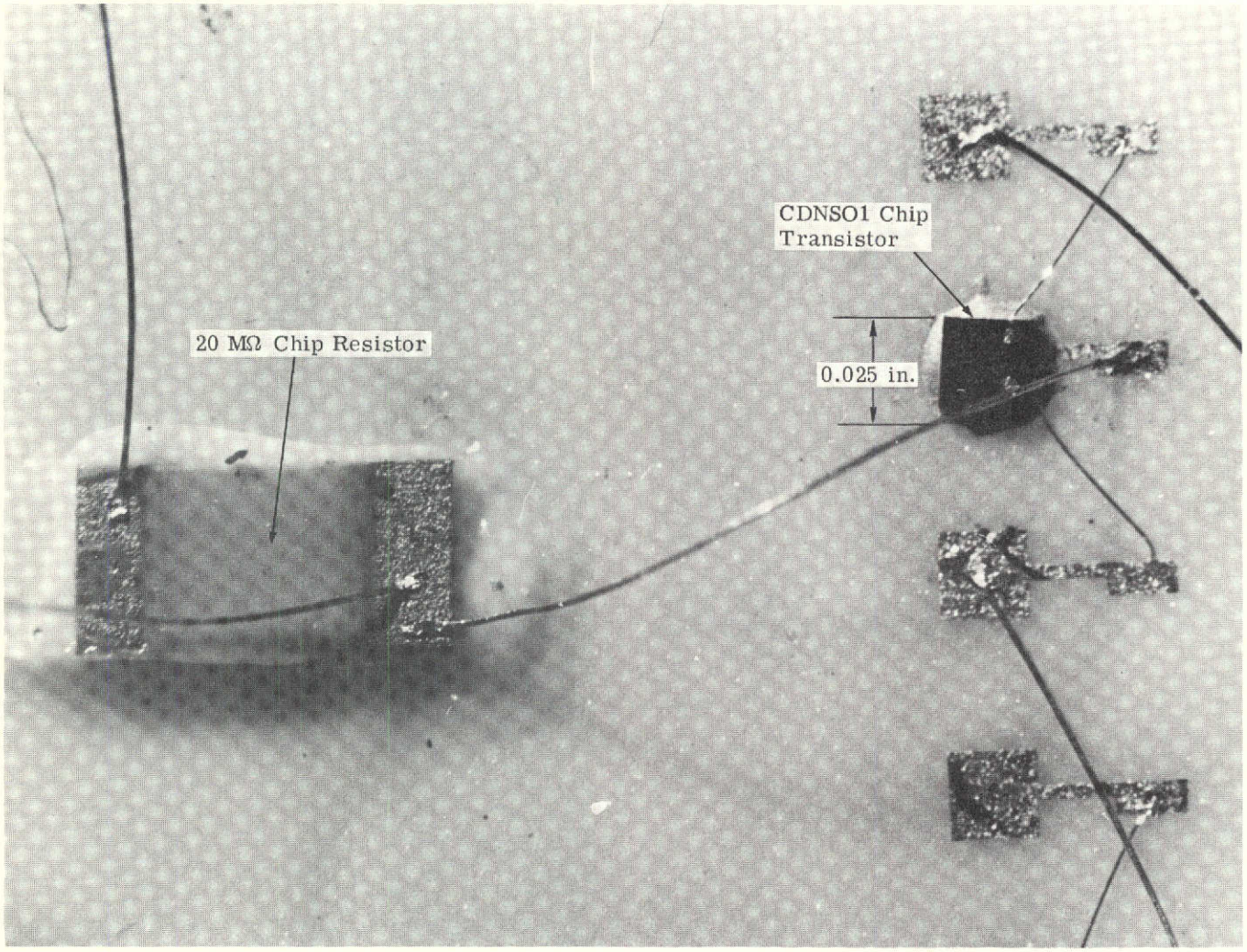

FIGURE 33. DETAILS OF HYBRID FIRST-STAGE BREADBOARD

Horizontal Sensitivity: 2 ms/cm

Vertical Sensitivity: 0.1 mV/cm

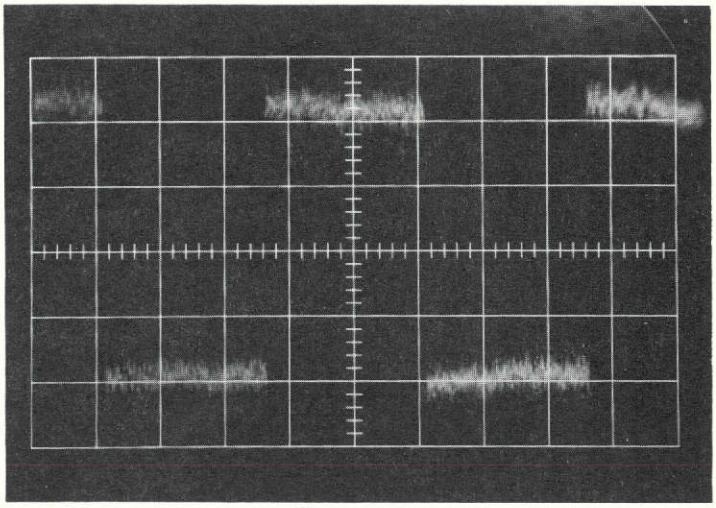

ORIGINAL

Horizontal Sensitivity: 2 ms/cm

Vertical Sensitivity: 2 mV/cm

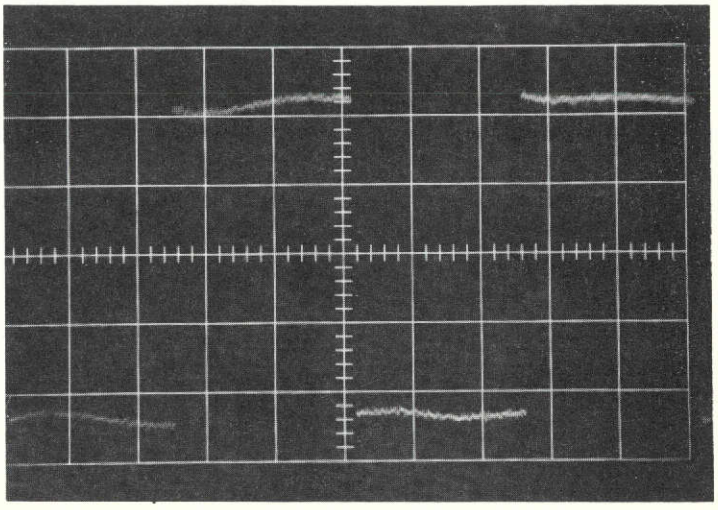

HYBRID

FIGURE 34. NOISE RESPONSE FROM ORIGINAL AND HYBRID PREAMPLIFIERS WITH THE SAME DETECTOR AND INPUT GEOMETRY. Source: 100 Hz squarewave form driving a GaAs diode.

REFERENCES

1. Wesley W. Wendlandt and Harry G. Hecht, Reflectance Spectroscopy, Interscience Publishers, New York, 1966, p. 256.
2. W. A. Malila, et al., Information Extraction Techniques for Multispectral Scanner Data, Report No. 31650-14-T, Willow Run Laboratories, Ann Arbor, June 1972, pp. 124-171.
3. Leo M. Larsen, Detector Utilization in Line Scanners, Report No. 31650-29-T, Willow Run Laboratories, Ann Arbor, August 1971, pp. 3-9.